CHAPTER V

RESULTS AND DISCUSSION

5.1 Investigation of oxygen species by fuel cell type temperature-programmed desorption (FC-TPD) measurement

Desorption of oxygen from a fuel cell unit was continuously observed under the constant rate of temperature increase (β) with helium flow at the anode side. Three kinds of TPD operation were conducted after three kinds of pretreatment. Proposed scheme for adsorption and desorption of oxygen on the anode of fuel cell system is summarized in Figure 5.1. For open circuit pretreatment, since the circuit is not connected, there is no oxygen permeation from the cathode side to the anode side. Oxygen adsorbed on the anode is from air feed stream at the anode side as shown in Figure 5.1-(a). However, a negligible amount of thermal migrations of oxygen ions through the solid electrolyte could occur at the high temperature condition.

When the circuit is closed during the pretreatment, the permeation of oxygen species is also allowed. Therefore, the closed circuit pretreatment provides the combined effect of oxygen adsorption from the surface and the permeation through the electrolyte as shown in Figure 5.1-(b). Especially, for the pretreatment under applied potential, it is expected that the amount and quality of the adsorption site should be altered as shown in Figure 5.1-(c).

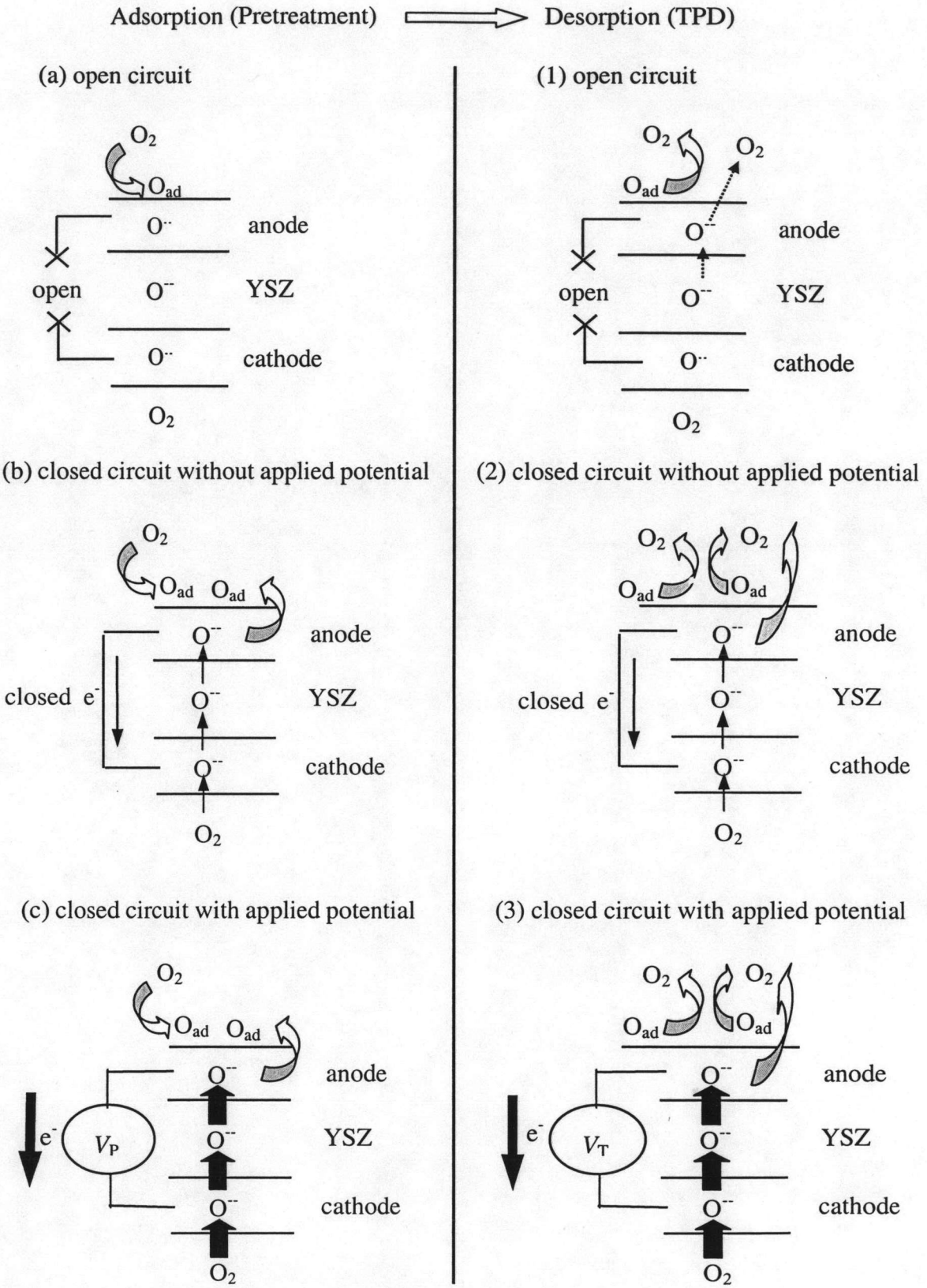

Figure 5.1 Proposed scheme for adsorption and desorption of oxygen on the anode of fuel cell system.

Figure 5.1-(1) shows the open circuit FC-TPD where surface oxygen species on the anode desorb without permeation of oxygen across the cell. The dotted line with arrow shows a possibility that a small amount of oxygen in YSZ electrolyte desorbs at high temperature. When the circuit is closed, the permeation of oxygen is also possible in addition to desorption of surface oxygen as shown in Figure 5.1-(2). For the closed circuit FC-TPD under applied potential, the rate of oxygen permeation should be promoted with the driving force of applied potential as shown in Figure 5.1-(3).

Table 5.1 lists FC-TPD experiments (case 1-8) at various operating modes of FC-TPD ((1)-(3) in Figure 5.1) and pretreatment conditions ((a)-(c) in Figure 5.1).

Table 5.1 Summary of FC-TPD experiments.

Case No.	Pretreatment Condition, V_P	Operating type of FC-TPD, V_T	Note
1	(a) open circuit	(1) open circuit	See Sec.5.2.1
2	(b) closed circuit, 0 V	(1) open circuit	See Sec.5.2.1
3	(c) closed circuit, 1 V	(1) open circuit	See Sec.5.2.1
4	(c) closed circuit, 2 V	(1) open circuit	See Sec.5.2.1
5	(a) open circuit	(2) closed circuit, 0 V	See Sec.5.2.2
6	(b) closed circuit, 0 V	(2) closed circuit, 0 V	See Sec.5.2.2
7	(c) closed circuit, 2 V	(2) closed circuit, 0 V	See Sec.5.2.2
8	(a) open circuit	(3) closed circuit, 1 V	See Sec.5.2.3

5.1.1 Open circuit FC-TPD

Open circuit FC-TPD measurements were carried out to investigate the nature of adsorbed oxygen on the anode catalyst of the fuel cell system (LSM/YSZ/LaAlO). Since the circuit was not connected, there was no oxygen permeation from the cathode side to the anode side. Therefore, the observed spectra are arisen from oxygen desorbed from the anode and the electrolyte as shown in Figure 5.1-(1). Figure 5.2 shows the effect of external applied potential during the pretreatment on FC-TPD spectra.

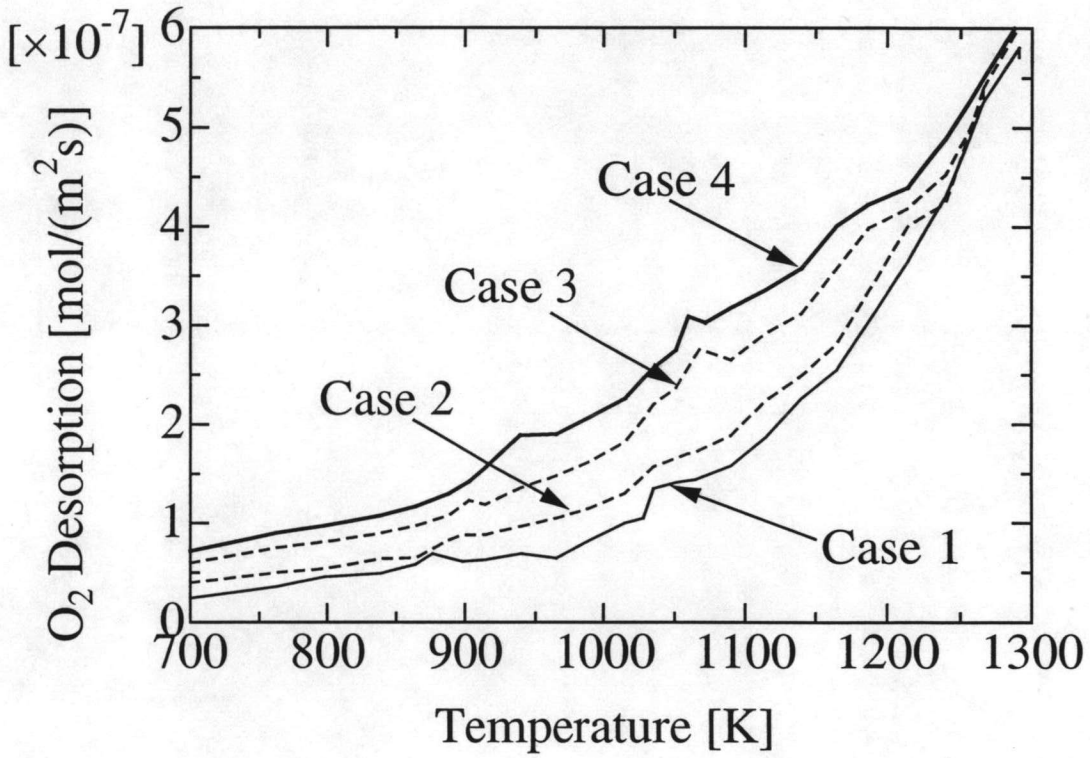

Figure 5.2 Effect of pretreatment condition on the open-circuit FC-TPD results (β = 0.117 K s^{-1}).

The pretreatment conditions included the open circuit pretreatment, Figure 5.1-(a) (Case 1), the closed circuit pretreatment, Figure 5.1-(b) (Case 2) and the closed circuit pretreatment with external applied potential, Figure 5.1-(c), V_P = 1 V (Case 3) and 2 V (Case 4). An internal potential, which corresponded to electromotive force of concentration cell conditions, existed even if no external potential was applied (V_P = 0 V) during the pretreatment. These values for the open circuit (Case 1) and closed circuit pretreatment (Case 2) at 1273 K were as high as 197 and 189 mV, respectively. These internal potentials at 1273 K were not changed during the pretreatment. It was found that the increase of the applied potential during the pretreatment increased the amount of desorbed oxygen especially at temperature lower than 1250 K. This suggests that the applied potential can activate the ability of the anode material (LaAlO) on oxygen adsorption.

Tagawa *et al.* (1998) performed TPD study of LaAlO powder, the anode catalyst of the system, they proposed that the oxygen species desorbed at low temperature (below 1000 K) were active for CO and CO_2 formation (oxygenate site) while the oxygen species desorbed at higher temperature (above 1000 K) were active for oxidative coupling of methane to C2-hydrocarbon (coupling site). Their two peaks at 930 K and 1120 K are corresponding to two peaks shown in Figure 5.2. By performing FC-TPD experiment with different values of temperature increase, the behavior of these two oxygen species can be revealed.

Figure 5.3 shows the effect of rate of temperature increase (β) on oxygen desorption in the open circuit mode for Case 1 (open circuit FC-TPD with open circuit pretreatment).

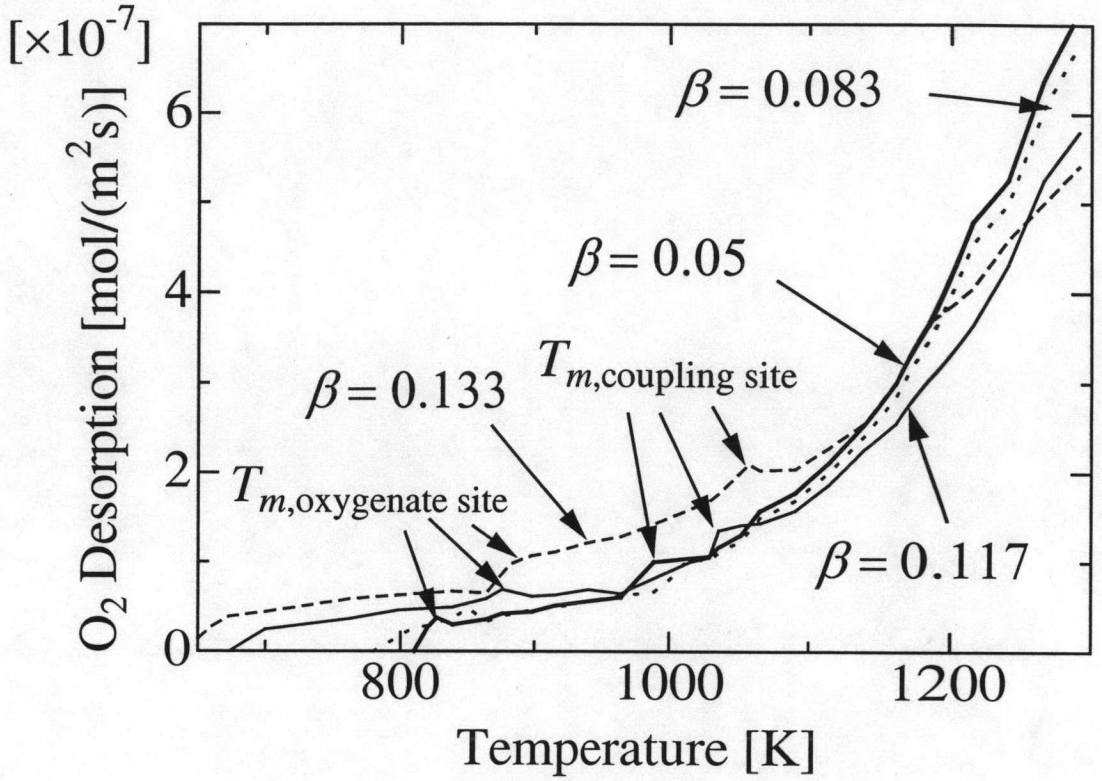

Figure 5.3 Effect of rate of temperature increase (β) on the results of the open circuit FC-TPD with the open circuit pretreatment (Case 1).

It is found that the temperatures for maximum amount of desorbed oxygen (T_m) of oxygenate site and coupling site are shifted to higher temperature with the increasing β. According to Cvetanovic and Amenomiya (1967), the activation energy of desorption (E_d) from TPD data with different β can be estimated by the following equation.

$$2\ln T_m - \ln(\beta) = \frac{E_d}{R_g T_m} + \ln\left(\frac{E_d}{A_d R_g}\right) \qquad (5.1)$$

With low rate of temperature increase (β), the operation time to a constant temperature increased and the intensity of oxygen at low temperatures became too low to be detected with our TCD. This suggested that a limited amount of oxygen species were desorbed between 700-800 K.

Figures 5.4 and 5.5 show the plot of Eq. (5.1) for the oxygenate site and the coupling site, respectively.

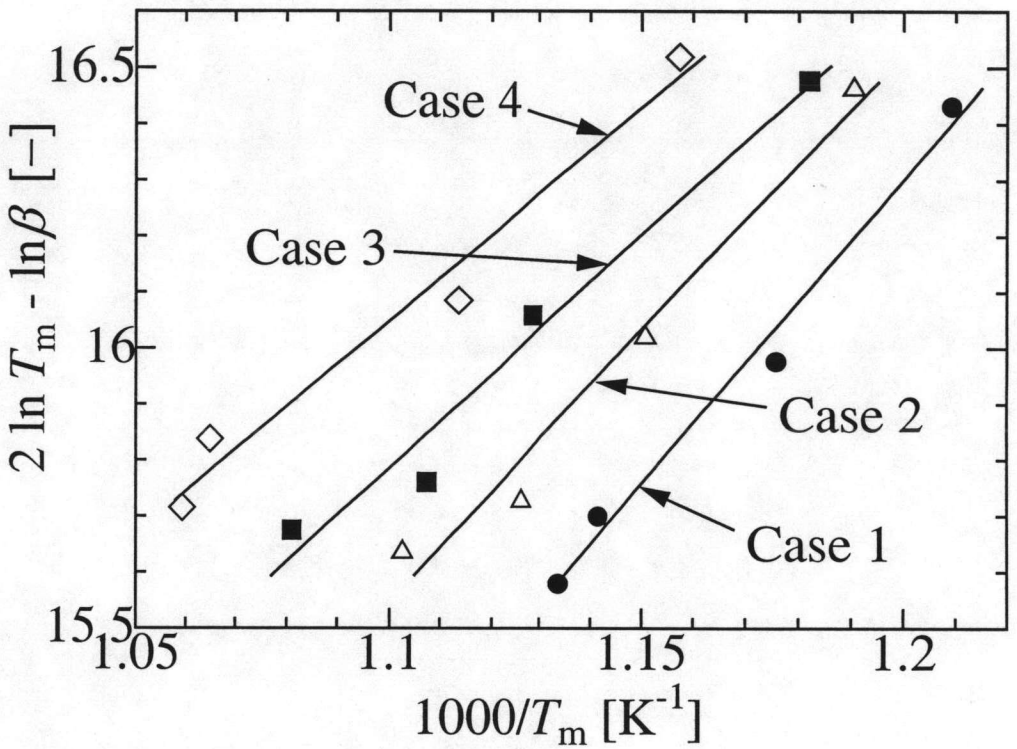

Figure 5.4 Plots of (2ln T_m – ln β) against 1000/T_m for oxygenate site in the open circuit FC-TPD mode.

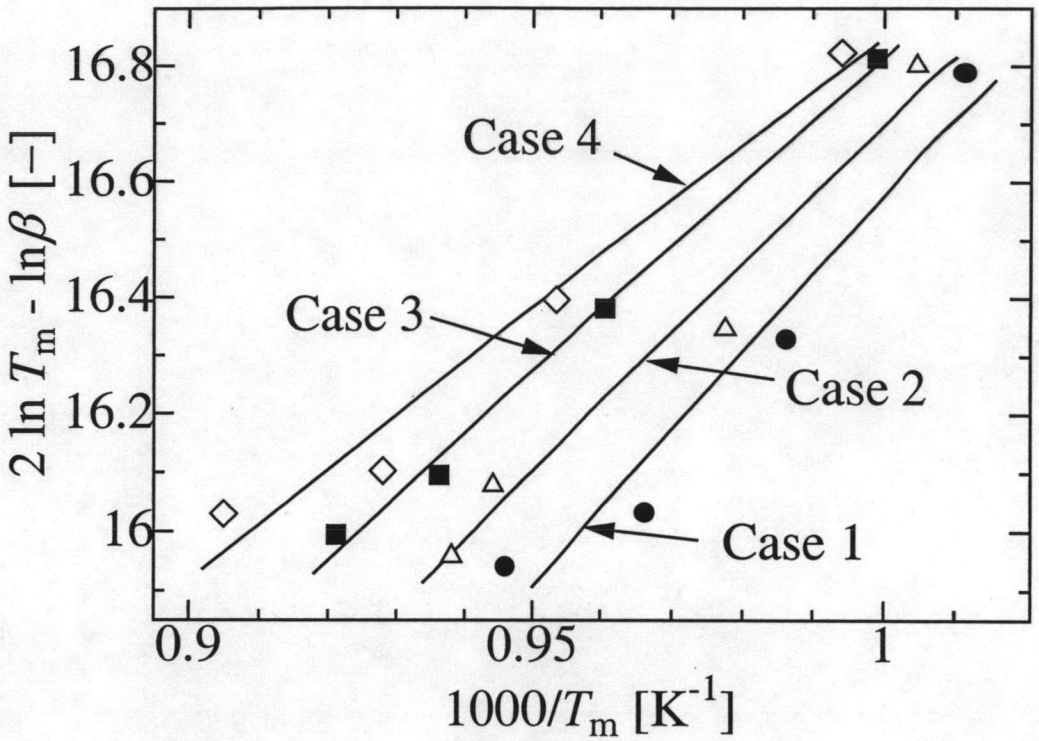

Figure 5.5 Plots of ($2\ln T_m - \ln \beta$) against $1000/T_m$ for coupling site in the open circuit FC-TPD mode.

The values of the activation energy of desorption for both sites are summarized in Table 5.2.

Table 5.2 Summary of activation energy of desorption at different levels of applied potential pretreatment condition from the open circuit FC-TPD measurements (Case 1-4).

Case No.	Oxygenate site		Coupling site	
	A_d (s^{-1})	E_d (kJ mol^{-1})	A_d (s^{-1})	E_d (kJ mol^{-1})
1	24.7	90	31.64	111
2	4.86	81	5.62	99
3	0.67	69	1.55	90
4	0.21	63	0.32	78

It is found that the activation energy of desorption decreases with increasing the applied potential during the pretreatment for both sites, suggesting the qualitative change of adsorption site with the electrostatic field.

Tsiplakides *et al.* (2000) and Neophytides and Vayenas (1995) also reported the changes in activation energy of oxygen desorption with applied potential on metal electrodes in the electrochemical system. They also pointed out the importance of these phenomena to understand the non-Faradic electrochemical modification of catalytic activity (NEMCA) effect. Pacchioni *et al.* (1996) suggested that this decrease in activation energy was largely due to electrostatic effected by considering interaction between the field induced by the ions and the polar metal-oxygen bond from their quantum chemical calculations. Vayenas *et al.* (2003) also suggested the back spillover mechanism on Pt electrode supported on YSZ from their scanning tunneling microscopy (STM) study. These discussions on precious metal surface could be applied to oxide electrode surface in this study to explain the decrease of activation energy of desorption with applied potential during pretreatment. The electrostatic effects arranged the active site to reduce metal-oxygen bonding even in the case of oxide type catalysts. Assuming that the transfer or adsorption of oxygen on these sites was possible during the pretreatment, results in Table 5.2 (open circuit FC-TPD) suggested that the oxygen species adsorbed on these arranged sites kept the weak metal ion-oxygen bonding after the electrostatic field was removed.

5.1.2 Closed circuit FC-TPD

When the circuit is closed during FC-TPD experiment, the permeation of oxygen species is also allowed. Therefore, the closed circuit FC-TPD mode provides the combined effect of oxygen desorption from the surface and oxygen permeation through the electrolyte as shown in Figure 5.1-(2).

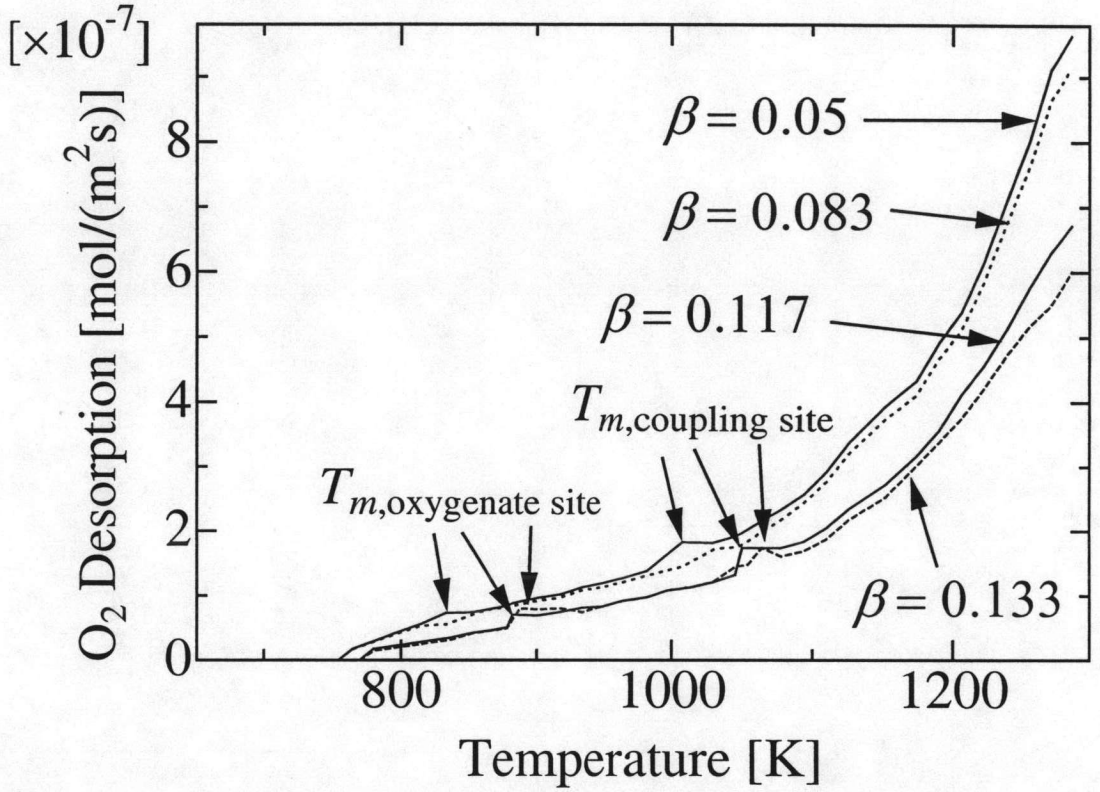

Figure 5.6 Effect of rate of temperature increase (β) on the results of the closed circuit FC-TPD with the open circuit pretreatment (Case 5).

The rate of temperature increase (β) was varied to obtain the activation energy. Figure 5.6 shows the effect of rate of temperature increase (β) on total oxygen desorption in the closed circuit mode with the open circuit pretreatment (Case 5).

Although, V_T is 0 V in the cases of 5-7, an internal potential as high as concentration cell existed during TPD operation. The value is estimated as high as 225 mV from steady state permeation experiments. Two peaks similar to those observed in the open circuit mode are found in this case.

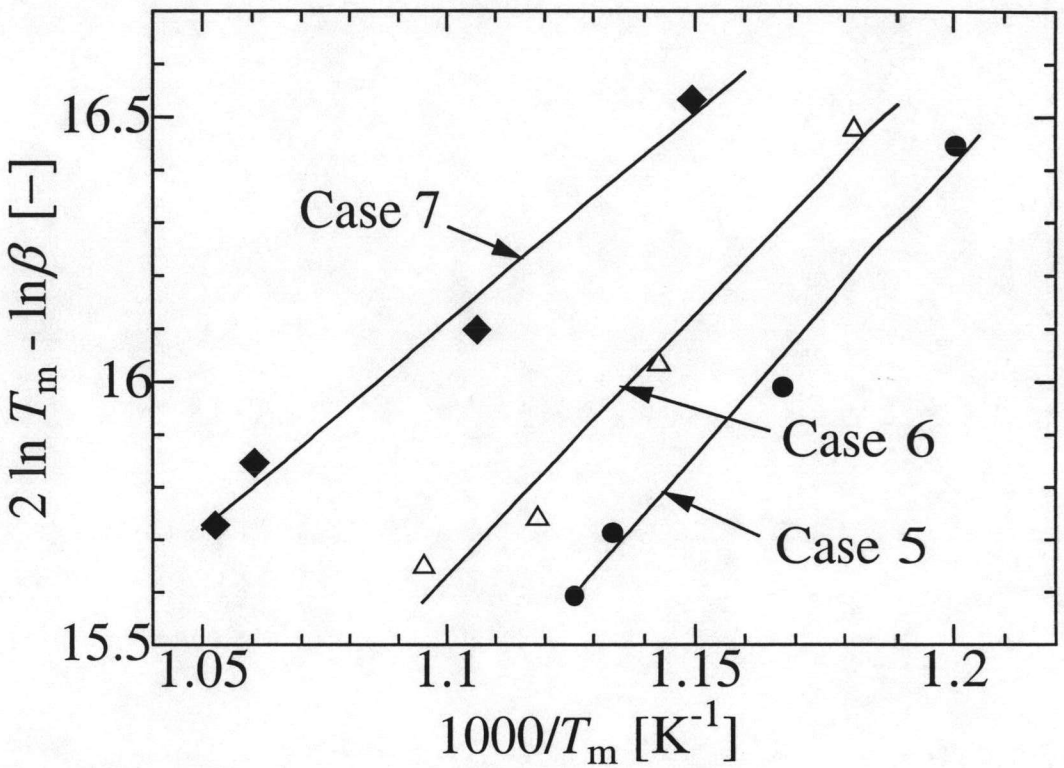

Figure 5.7 Plots of (2ln T_m – ln β) against 1000/T_m for oxygenate site in the closed circuit FC-TPD mode.

Oxygen desorption increases with decrease of β. This may be due to the effect of oxygen permeation through cell system.

Figures 5.7 and 5.8 show plots of Eq. (5.1) for the oxygenate site and the coupling site, respectively.

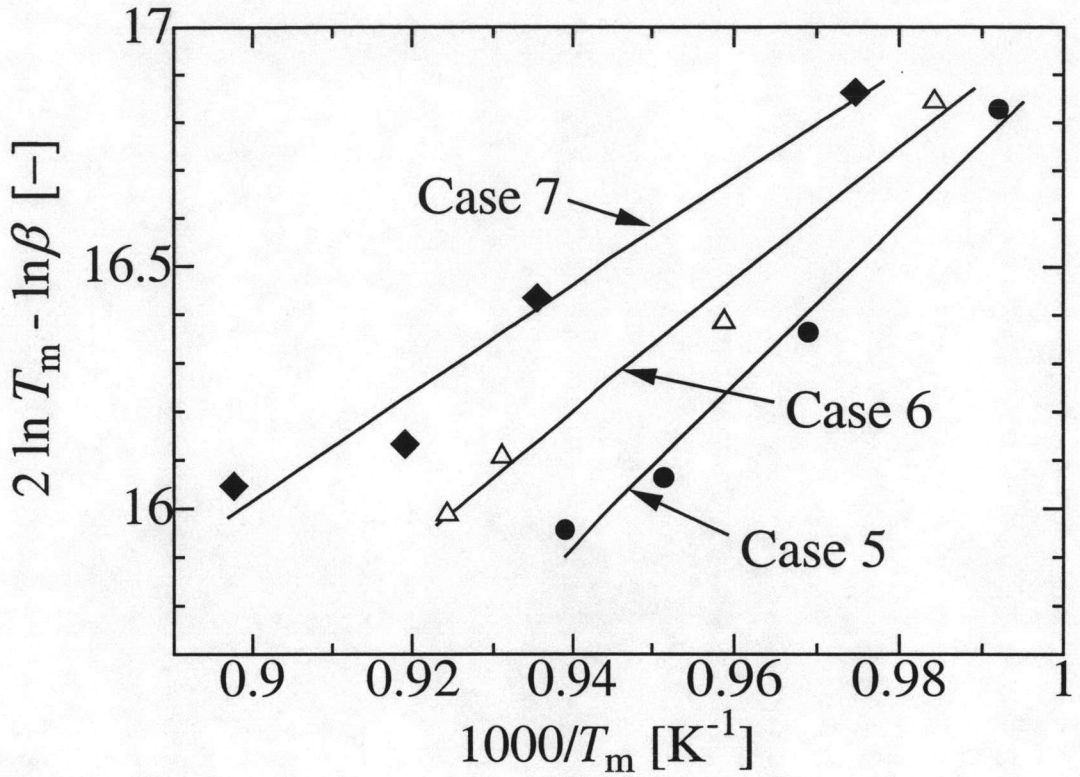

Figure 5.8 Plots of ($2\ln T_m - \ln \beta$) against $1000/T_m$ for coupling site in the closed circuit FC-TPD mode.

The values of the activation energy for both sites are summarized in Table 5.3. Similar to the open circuit FC-TPD, the activation energy decreases with increasing the applied potential during pretreatment for both sites. This also suggests the qualitative change of adsorption site with the electrostatic field.

Table 5.3 Summary of activation energy at different levels of applied potential pretreatment condition from the closed circuit FC-TPD measurements (Case 5-7).

Case No.	Oxygenate site		Coupling site	
	A_d (s^{-1})	E_d (kJ mol^{-1})	A_d (s^{-1})	E_d (kJ mol^{-1})
5	0.46	92	14.49	140
6	0.09	83	0.48	112
7	$4.47x10^{-3}$	65	0.03	93

The activation energies of the oxygenate site with the open circuit and closed circuit operation modes are almost the same. On the other hand, the activation energy of the coupling site from the closed circuit mode is much higher than that from the open circuit mode. The reason will be discussed later in Section 5.2.2.

5.1.3 Closed circuit FC-TPD with external applied potential

Tagawa *et al.* (2003) studied the effects of applied potential on the rates of oxidative coupling of methane in the SOFC reactor. As shown in Figure 5.9, the external potential was applied when mixture of air and methane was fed on the anode (air + CH_4/LaAlO/YSZ/LSM/O_2). When the circuit was closed with no applied potential, the rate of CO_2 formation was significantly decreased and CO formation rate was increased while C2 formation was almost the same. The similar tendency was observed with applied potential. These effects of applied potential could not be explained by "Faraday's Law". Therefore, they proposed these effects as NEMCA phenomena (Tagawa *et al.*, 2003).

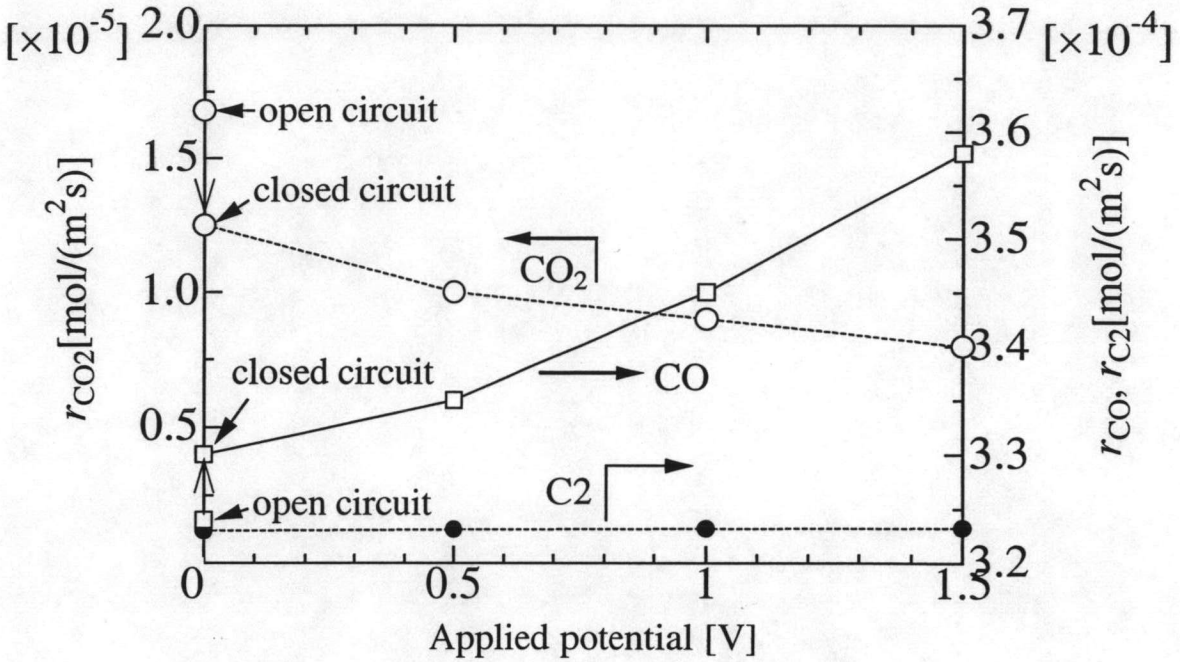

Figure 5.9 Effect of applied potential on rates of formation of products (T = 1223 K) (pre-mixed feed of oxygen (2.4×10^{-6} mol s^{-1}) and methane (5.1×10^{-5} mol s^{-1}) in the anode side and oxygen feed (6.8×10^{-6} mol s^{-1}) in the cathode side).

These behaviors can be explained by considering the results from the closed circuit FC-TPD with and without external applied potential (Case 5 and Case 8, respectively). As shown in Figure 5.1-(3), with external applied potential, the qualitative change in adsorption site may be induced as discussed in the previous section at low temperature. Permeation of oxygen is also enhanced at high temperature with applied potential as shown in Figure 5.10.

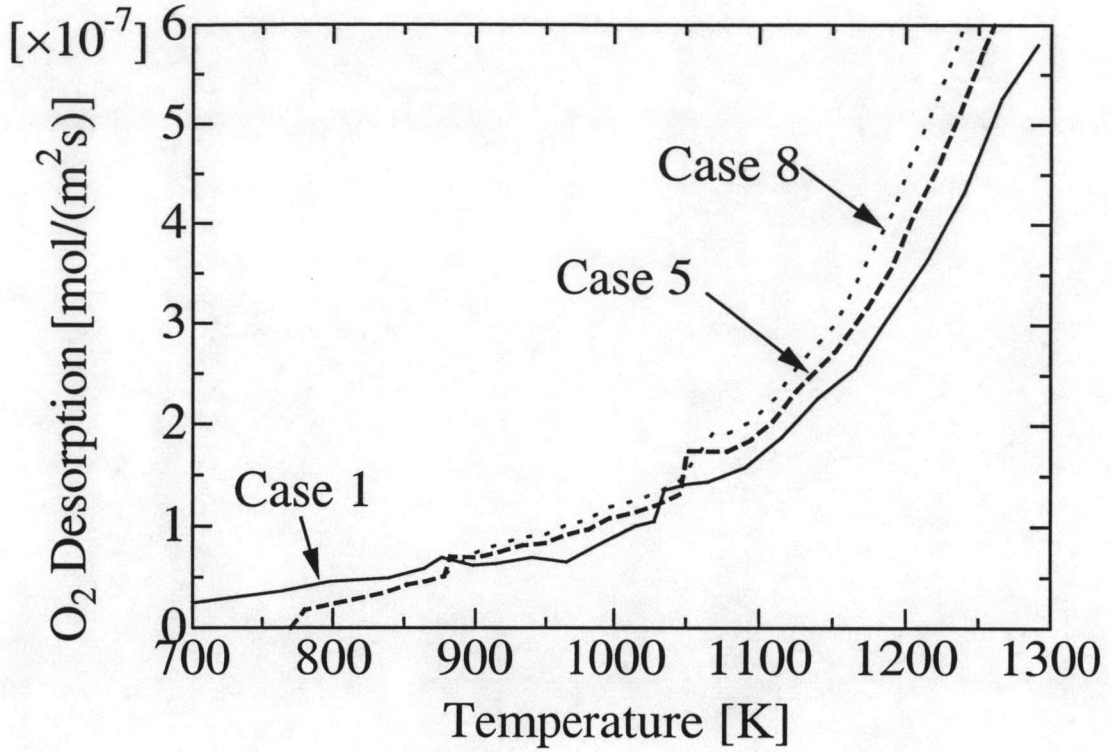

Figure 5.10 Effect of applied potential on FC-TPD results (open circuit pretreatment, $\beta = 0.117$ K s^{-1}).

Oxygen starts to desorb below 700 K with open circuit mode (Case 1), but the temperature shifts to 800 K when the circuit is closed (Case 5). The amount of desorbed oxygen species at 1000 K from the closed circuit mode dominates the open circuit mode. Similar tendency is observed when the external potential ($V_T = 1$ V) was applied (Case 8). Assuming that loosely bound oxygen species (the one that desorbs at T = 700-800 K) is active for the combustion reaction (CO_2 formation), an increase of interaction between adsorbed oxygen species and the anode by applied potential (species desorbed at 800-1000 K) reduces the activity of oxygen species to form oxygenates and the combustion hardly occurs, resulting in the production of CO. NEMCA effect shown in Figure 5.9 can be correlated to the behavior of active site to interact with oxygen under the electrostatic field.

5.2 Oxygen permeation study

5.2.1 Oxygen transport model

(a) Oxygen permeation through thin YSZ membranes modeled by Han et al. (1997)

Goto *et al.* (2003) studied the simulation on micro fuel cell system; they have referred an oxygen permeation model presented by Han *et al.* (1997). The proposed permeation process is summarized in Figure 5.11. In their study, a thin YSZ membrane prepared by the electrochemical vapor deposition (EVD) method was employed. The oxygen permeation flux can be described by the following equations (Han *et al.*, 1997).

At gas-membrane interface of the cathode side:

$$J_{O_2} = \alpha\left(P_{\text{rich}}^{1/2} - P_{O_2(\text{I})}^{1/2}\right) \tag{5.2}$$

In bulk oxide of YSZ:

$$J_{O_2} = \frac{\delta}{L}(P_{O_2(\text{I})}^{1/4} - P_{O_2(\text{II})}^{1/4}) \tag{5.3}$$

At membrane-gas interface of the anode side:

$$J_{O_2} = \alpha\left(P_{O_2(\text{II})}^{1/2} - P_{\text{lean}}^{1/2}\right) \tag{5.4}$$

The rate parameters α and δ at T = 1173 K are $9.4\text{x}10^{-7}$ mol m^{-2} s^{-1} $Pa^{-1/2}$ and $5.2\text{x}10^{-11}$ mol m^{-1} s^{-1} $Pa^{-1/4}$, respectively. The activation energy of α and δ are 53.1 and 72.0 kJ mol^{-1} K^{-1}, respectively. As shown in Figure 5.11, this system was operated under open circuit without the anode and cathode electrodes. 1% of hydrogen in helium was used as a reacting sweep gas. These conditions were not the same as our present system, which was operated under closed circuit with or without applied potential with LSM as the cathode and LaAlO as the anode catalyst.

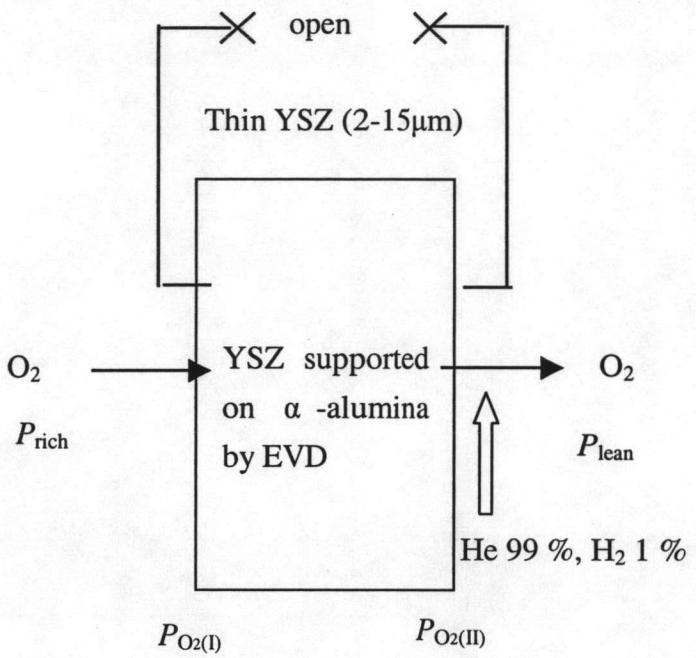

Figure 5.11 Oxygen permeation process through thin YSZ membranes prepared by the electrochemical vapor deposition (EVD) method supported on α-alumina reported by Han *et al.* (1997).

(b) A model for the oxygen permeation through the LSM/YSZ/LaAlO

In this study, an oxygen permeation model through the LSM/YSZ/LaAlO fuel cell type reaction system with closed circuit and applied potential is proposed. Schematic models of oxygen permeation are shown in Figure 5.12. The circuit was closed to allow the electron transfer. Two kinds of carrier gas were used: i.e. helium (Figure 5.12-(a)) and methane (Figure 5.12-(b)).

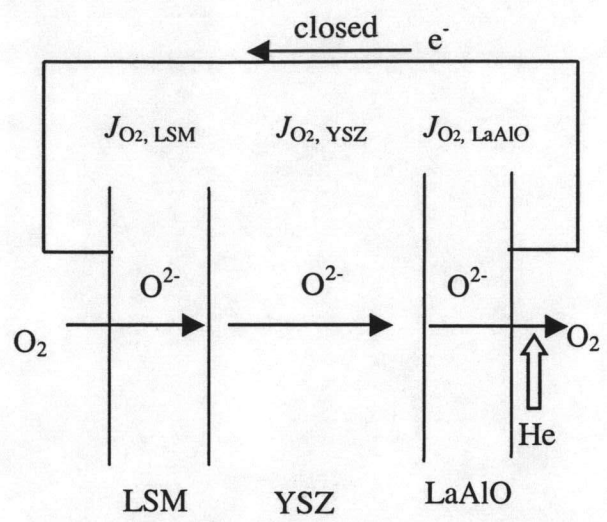

a) Helium feed at anode, closed circuit without applied potential

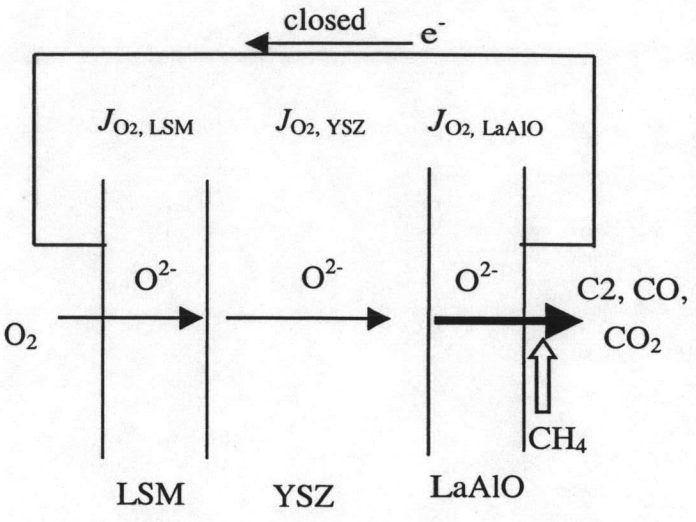

b) Methane feed at anode, closed circuit without applied potential

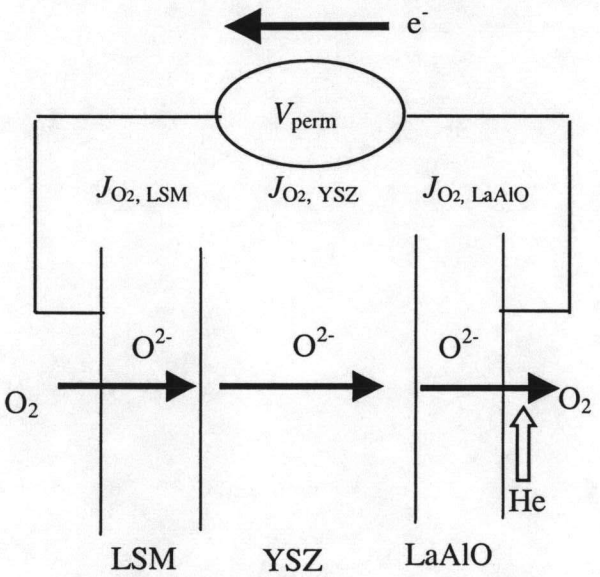

c) Helium feed at anode, closed circuit with applied potential

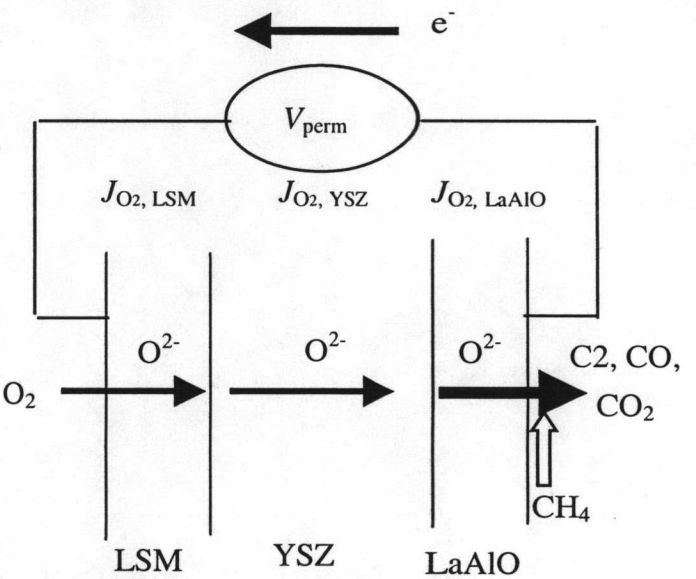

d) Methane feed at anode, closed circuit with applied potential

Figure 5.12 Proposed schemes for oxygen permeation through LSM/YSZ/LaAlO at various conditions.

- *In the case of helium feed without applied potential*

Figure 5.12-(a) shows general reaction paths as follows: 1) electrochemical reduction at the LSM surface to form oxygen ions, 2) incorporation of oxygen ions into the YSZ lattice, 3) recombination and desorption of oxygen ions to form oxygen molecules at the LaAlO anode.

The permeation of oxygen through a electrochemical media depends upon ionic conductivity (σ_i) and electronic conductivity (σ_e) of the media. Assuming surface concentration of oxygen ions is equilibrated with gas phase, they can be estimated from the following equations (Kharton *et al.*, 2000).

$$J_{O_2} = \frac{Per_{,O_2}}{L} \ln\left(\frac{P_{rich}}{P_{lean}}\right) \quad (5.5)$$

$$Per_{,O_2} = \frac{R_g T}{16F^2} \frac{\sigma_i \sigma_e}{\sigma_i + \sigma_e} \quad (5.6)$$

$$\sigma_j = \left(\frac{A_j}{T}\right) \exp\left(\frac{-E_j}{R_g T}\right); j = i, e \quad (5.7)$$

The ionic conductivities of LSM ($\sigma_{i\text{-LSM}}$) (Yasuda *et al.*, 1996), the electronic conductivities of LSM ($\sigma_{e\text{-LSM}}$) (Li *et al.*, 1993; Kharton *et al.*, 2003), the ionic conductivities of YSZ ($\sigma_{i\text{-YSZ}}$) (Badwal, 1992) and the electronic conductivities of YSZ ($\sigma_{e\text{-YSZ}}$) (Xia *et al.*, 2000) were cited from the literatures and the values are summarized in Table 5.4.

Table 5.4 Values of parameters for the calculations of oxygen permeation flux.

Parameters	A_j (S K m^{-1})	E_j (kJ mol^{-1})	Ref.
$\sigma_{i\text{-LSM}}$ (S m^{-1})	2.311x10^{11}	284	Yasuda *et al.*, 1996 [a]
$\sigma_{e\text{-LSM}}$ (S m^{-1})	8.855x10^{7}	9	Li *et al.*, 1993 [b], Kharton *et al.*, 2003 [c]
$\sigma_{i\text{-YSZ}}$ (S m^{-1})	7.121x10^{7}	88	Badwal, 1992
$\sigma_{e\text{-YSZ}}$ (S m^{-1})	9.244x10^{5}	87.5	Xia *et al.*, 2000

L_{LSM} = 1x10^{-6} m, L_{YSZ} = 1.5x10^{-3} m, L_{LaAlO} = 5x10^{-6} m.

a) From Table 1 at 1173 K, the value was interpolated between $La_{0.95}Sr_{0.05}MnO_3$ and $La_{0.8}Sr_{0.2}MnO_3$, and at 1273 K between $La_{0.9}Sr_{0.1}MnO_3$ and $La_{0.8}Sr_{0.2}MnO_3$.

b) $\sigma_{e\text{-LSM}}$ was given at 1173 K.

c) The activation energy was shown in Table 1.

However, these values of LaAlO are not available in literature. Due to the recombination and desorption of oxygen ions to form oxygen molecules at LaAlO anode, the overall rate of these processes at LaAlO might be estimated from Eq. (5.8)

$$J_{O_2} = k_{O_2\text{-perm}} \ln\left(\frac{P_{rich}}{P_{lean}}\right) \qquad (5.8)$$

where P_{rich} and P_{lean} represent partial pressures of oxygen at the rich and lean sides of LaAlO, respectively.

When the permeation is at steady state, the oxygen permeation flux across different parts of the cell is equal to the observed experimental results.

$$J_{O_2,Exp} = J_{O_2,LSM} = J_{O_2,YSZ} = J_{O_2,LaAlO} \qquad (5.9)$$

The values of $k_{O2\text{-}perm}$ of LaAlO at different temperatures were determined by using an all-purpose equation solver, EQUATRAN-G (Omega Simulation, Japan). P_{rich} of LSM is partial pressure of oxygen at feed side (=101.3 kPa) while P_{lean} of LaAlO is partial pressure of oxygen at permeate side which calculated from the experiments. The estimated $k_{O2\text{-}perm}$ value was shown as follows.

$$k_{O_2-perm} = 0.413 \exp\left(\frac{-170400}{R_g T}\right) \qquad (5.10)$$

- *In the case of methane feed without applied potential*

Oxygen ions directly reacted with methane at the anode (Figure 5.12-(b)). It was expected that the oxygen permeation rate could be enhanced. Due to the chemical reaction at the anode catalyst surface, the overall reaction rate could depend on partial pressure of methane and surface oxygen concentration. The oxygen surface reaction coefficient ($k_{O2\text{-}Rxn}$) was estimated from experimental oxygen permeation flux by the following equation.

$$J_{O_2} = k_{O_2-Rxn} P_{CH_4} \ln\left(\frac{P_{rich}}{P_{lean}}\right) \qquad (5.11)$$

No oxygen was observed in gas phase of the permeate side due to reactions with methane. The surface oxygen may not be in the equilibrium with oxygen in gas phase. However, the surface oxygen concentration in methane feed could be assumed similar to the helium case. Therefore, P_{lean} in the helium case was used in Eq. (5.11)

- *In the case of closed circuit with applied potential*

It was expected that the oxygen transfer could be accelerated with increasing applied potential ((c)-(d) in Figure 5.12). Linear relationship between applied potential and oxygen permeation flux was assumed and the following equation could be proposed.

$$J_{O_2} = J_{O_2,0V} + k_V V_{Per} \qquad (5.12)$$

The values of $J_{O2,0V}$ without applied potential can be calculated by Eqs. (5.5)-(5.7) and (5.8) for the helium feed case and by Eqs. (5.5)-(5.7) and (5.11) for the methane feed case, respectively.

5.2.2 Steady state oxygen permeation results

(a) Helium feed

Figure 5.13 shows the effect of the applied potential on the oxygen flux at various temperatures. Linear relationships between the oxygen permeation flux and the applied potential were observed for all different temperatures. As shown in Figure 5.13, the oxygen could be permeated without applied potential due to the system possessed an internal "concentration cell" potential as a driving force. For example, the concentration cell potential is 0.225 V at 1223 K. This value agrees well with OCV value calculated from Nernst equation.

$$E = \frac{R_g T}{4F} \ln\left(\frac{P_{feed}}{P_{perm}}\right) \qquad (5.13)$$

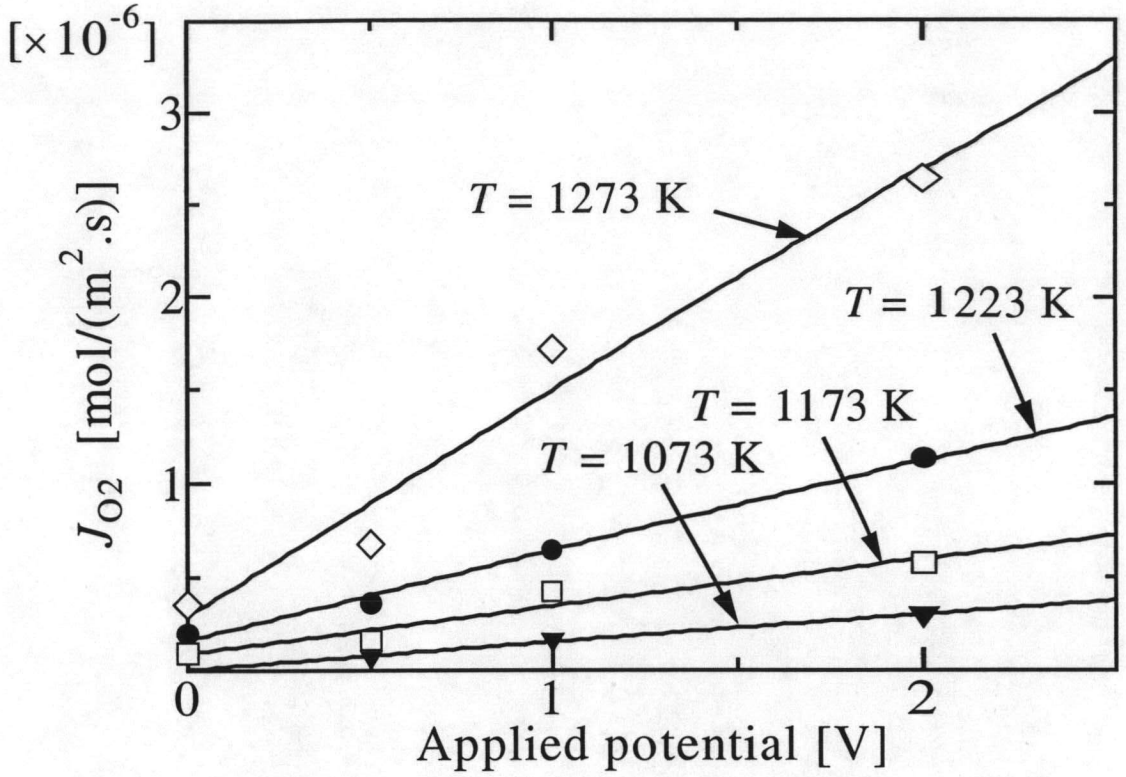

Figure 5.13 Effect of applied potential on oxygen flux at various temperatures by steady state permeation experiments using helium feed on the anode side.

Therefore, we can assume surface oxygen concentration at the lean side of LaAlO is in equilibrium with oxygen in gas phase at the permeate side.

The proportional constants (k_v) from Eq. (5.12) could be determined from the slopes and expressed as Eq. (5.14).

$$k_{V,He} = 0.102 \exp\left(\frac{-122700}{R_g T}\right) \qquad (5.14)$$

Figure 5.14 shows the plots between ln (J_{O_2}) and 1000/T at different levels of the applied potential. The solid lines represent the results calculated from Eqs. (5.5)-(5.8),

(5.12) and (5.14). The oxygen flux increases with the increasing temperature and applied potential.

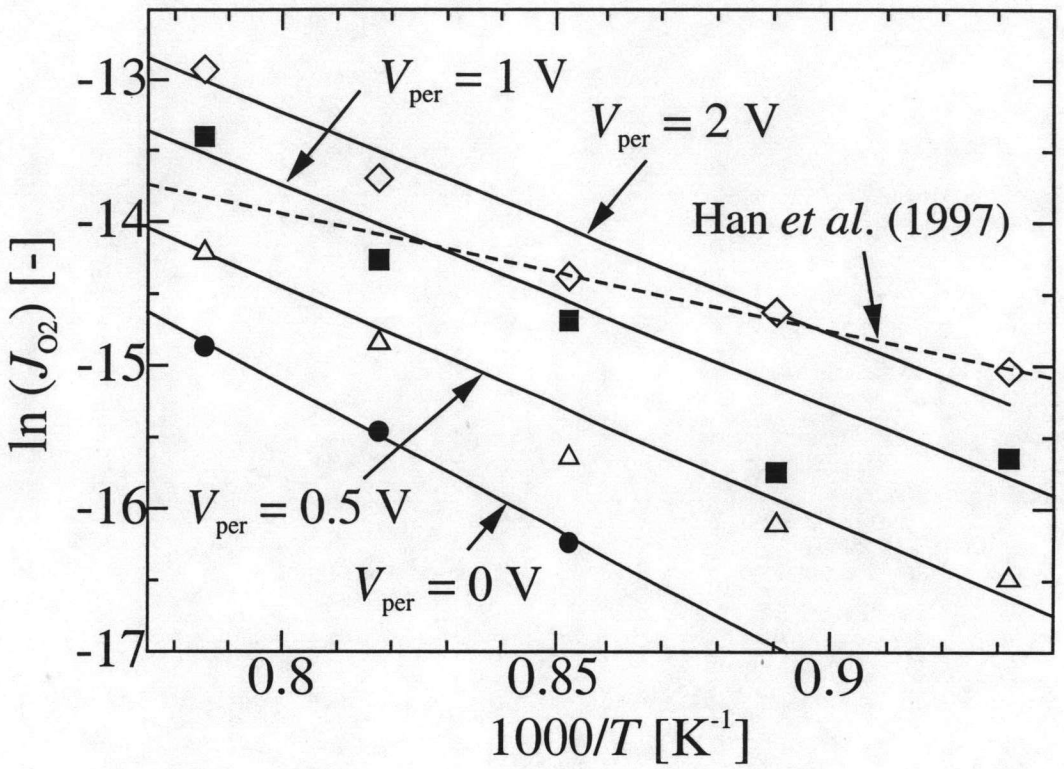

Figure 5.14 Arrhenius' plot between ln (J_{O_2}) and 1000/T at different levels of applied potential by steady state permeation experiments using helium feed on the anode side.

The solid lines in Figure 5.14 can be approximated by straight lines of Arrhenius' plots by Eq. (5.15).

$$J_{O_2} = A_{Per} \exp\left(\frac{-E_{Per}}{R_g T}\right) \qquad (5.15)$$

The overall activation energy of the oxygen transport through the cell (E_{Per}) was calculated from the slopes and the results are shown in Table 5.5.

Table 5.5 Summary of the values of pre-exponential factors of oxygen permeation and activation energy at different levels of applied potential from steady state permeation results using helium feed at anode side.

V_{Per} (V)	A_{Per} (mol m^{-2} s^{-1})	E_{Per} (kJ mol^{-1})
0	3.499	170
0.5	1.280	154
1	0.675	144
2	0.157	119

The activation energy is decreased from 170 kJ mol^{-1} in case of closed circuit with no applied potential to 119 kJ mol^{-1} with applied potential 2 V. From TPD experiments have shown that the applied potential also decreased the activation energy of the oxygen desorption. However, as mentioned above in Section. 5.1.2, the activation energies of the oxygenate site with the open circuit and closed circuit operation modes are almost the same. On the other hand, the activation energy of the coupling site from the closed circuit mode is much higher than that from the open circuit mode. As far as YSZ is concerned, the oxygen permeation at temperature lower than 1000 K can be neglected. Therefore, the desorption from oxygenate site ($T < 1000$ K) is not affected by oxygen permeation. However, at higher temperature above 1000 K, the permeation through YSZ cannot be neglected. This permeation may predominate and induce the activation energy of the oxygen desorption of coupling site increase from 111 to 140 kJ mol^{-1} in open circuit and closed circuit mode, respectively.

The dashed line in Figure 5.14 shows the results calculated from Han's model (Han *et al.*, 1997). The comparison of our model with Han's model will be described

later (Section 5.2.5).

(b) Methane feed

Instead of helium, methane was fed to the anode chamber to react with the permeating oxygen. At 1273 K, the electromotive force from the experiment is 1.09 V, which is near to the theoretical value of ethylene formation (1.05 V). Linear relationships between the oxygen permeation flux and the applied potential were observed for all different temperatures as shown in Figure 5.15.

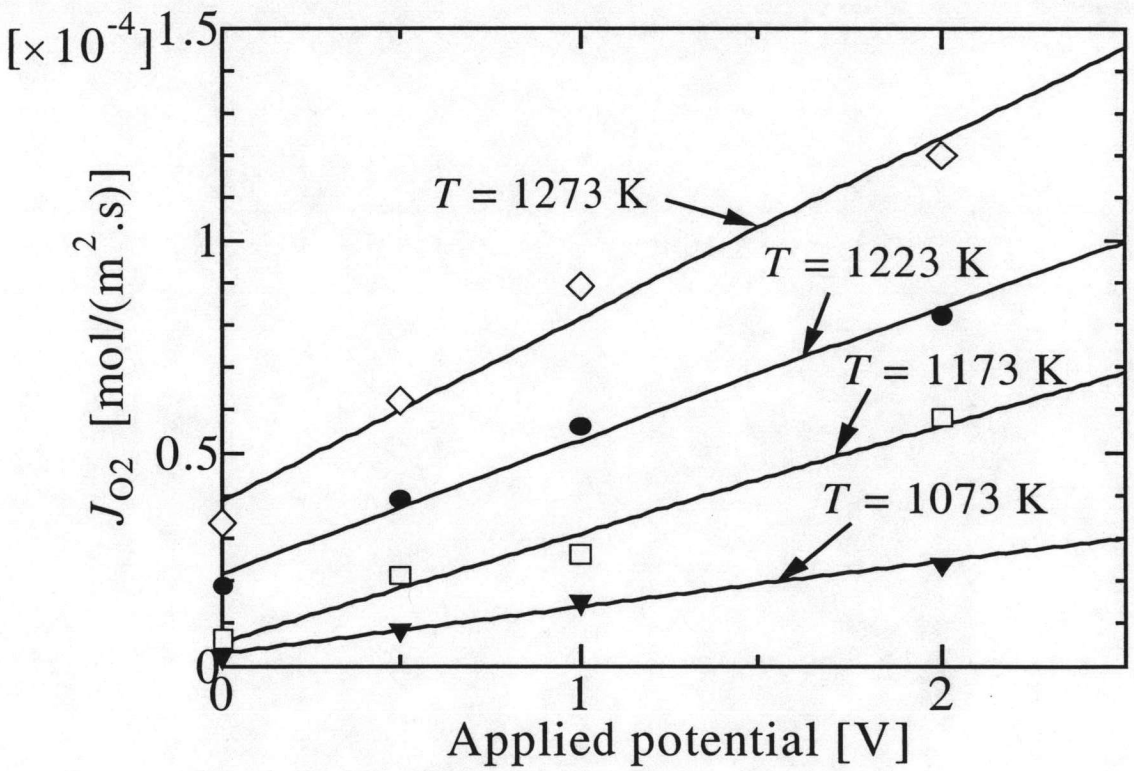

Figure 5.15 Effect of applied potential on oxygen flux at various temperatures by steady state permeation experiments using methane feed on the anode side.

The proportional constants (k_v) from Eq. (5.12) could be determined from the slopes and the expression is shown in Eq. (5.16).

$$k_{V,CH_4} = 0.875\exp\left(\frac{-104150}{R_g T}\right) \qquad (5.16)$$

Figure 5.16 shows the plots between ln (J_{O2}) and 1000/T at different levels of the applied potential. The oxygen flux with the methane feed was estimated from the equivalent rate of oxygen required for the oxidation reaction.

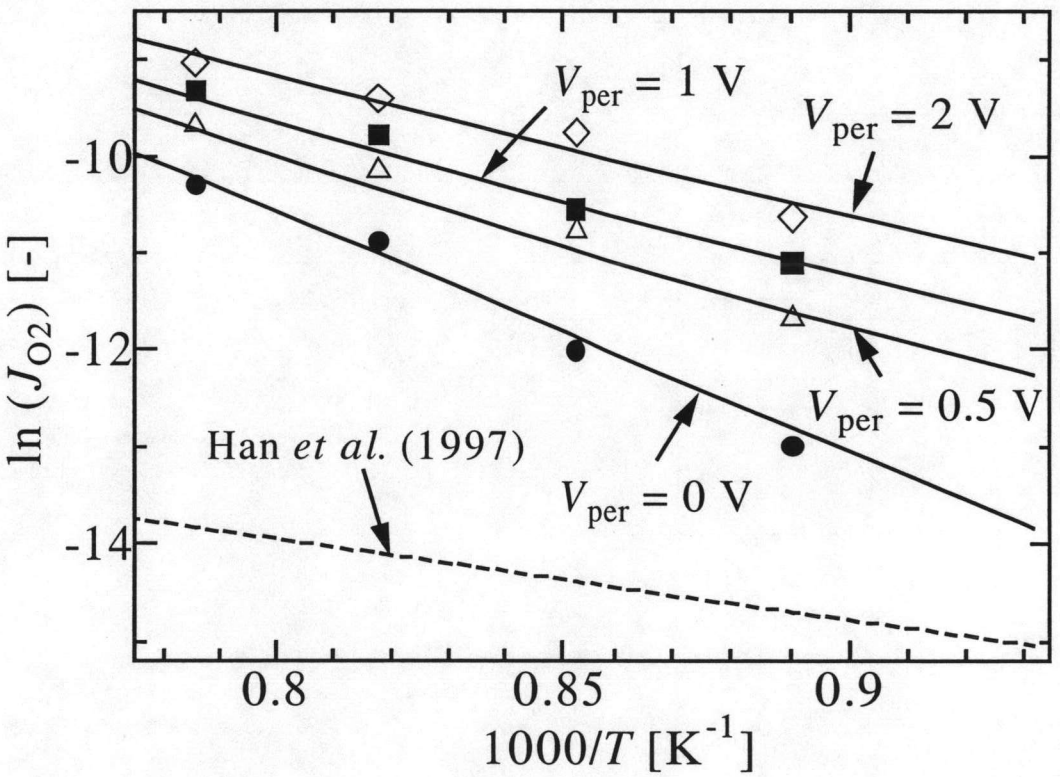

Figure 5.16 Arrhenius' plot between ln (J_{O2}) and 1000/T at different levels of applied potential by steady state permeation experiments using methane feed on the anode side.

The oxygen surface reaction coefficient ($k_{O2\text{-}Rxn}$) estimated from the experimental oxygen permeation flux by using Eq. (5.11) was shown as follows.

$$k_{O_2-Rxn} = 8.577x10^{-3} \exp\left(\frac{-195100}{R_g T}\right) \qquad (5.17)$$

The solid line with V_{Per} = 0 V represents the calculated results by Eqs. (5.5)-(5.7), (5.11) and (5.17). The solid lines for V_{Per} = 0.5 V, 1 V and 2 V were calculated by Eqs. (5.5)-(5.7), (5.11)-(5.12) and (5.16)-(5.17).

The solid lines in Figure 5.16 can be approximated by straight lines of Arrhenius' plots by Eq. (5.15). The overall activation energy of the oxygen transport through the cell (E_{Per}) was calculated from the slopes and the results are shown in Table 5.6. The applied potential increases the oxygen flux and also decreases the activation energy of the oxygen transport.

Table 5.6 Summary of the values of pre-exponential factors of oxygen permeation and activation energy at different levels of applied potential from steady state permeation results using methane feed at anode side.

V_{Per} (V)	A_{Per} (mol m^{-2} s^{-1})	E_{Per} (kJ mol^{-1})
0	3.632x10^4	219
0.5	186.9	157
1	82.84	145
2	15.77	124

Compared with the helium feed case, the oxygen flux is significantly improved when methane is fed to the anode side. The oxygen permeation fluxes under the methane feed are 1-2 orders of magnitude higher than those under the helium feed. It is clear that the reaction of methane with the permeated oxygen at the anode catalyst significantly improves the overall oxygen permeation flux due to the surface oxygen kinetics with methane. The dashed line in Figure 5.16 represents Han's model.

5.2.3 Oxygen partial pressure profiles and permeation mechanism

Figure 5.17 shows the oxygen partial pressure profile from the simulation results at 1223 K.

In the case of the helium feed (solid line), it is obvious that the major oxygen permeation resistance through the cell or the rate-limiting step of this system is at LaAlO electrode. Although the thickness of YSZ electrolyte is much more than the electrodes, the resistance of YSZ electrolyte is negligible. With the methane feed case (dashed lines), the resistances of three steps are comparable; consequently, the rate steps at the cathode and the electrolyte need to be taken into account.

In the case without methane, oxygen ions release electrons and recombine into oxygen molecules, which are then desorbed into the gas phase. On the other hand, with the methane feed, oxygen ions could directly react with methane to form CO_2, CO and C2 hydrocarbons.

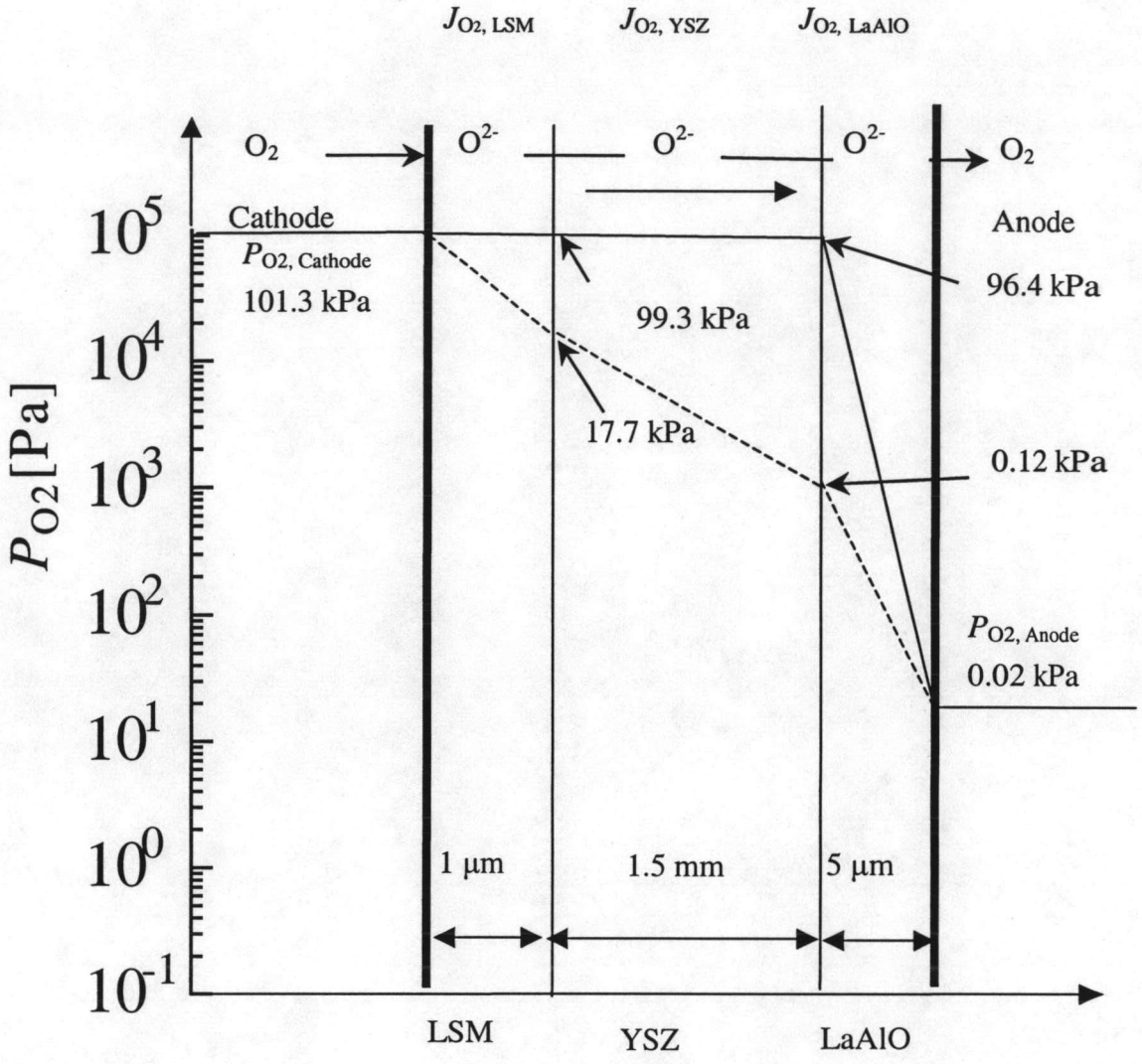

Figure 5.17 The mechanism of oxygen permeation and the profile of oxygen partial pressure in LSM/YSY/LaAlO from the simulation results at 1223 K (solid line: helium feed, dashed line: methane feed).

Mechanisms of the oxygen activation on LSM and the bulk transport of O^{2-} in YSZ might be the same as the helium feed case as shown in the previous sections. The change in the surface reaction step on the anode from the recombination and desorption of oxygen ion to the reaction of oxygen species with methane would be the main reason for the increase of oxygen flux for the methane feed.

5.2.4 Effect of YSZ thickness

The effect of YSZ thickness on the oxygen permeation flux is simulated and the results are shown in Figure 5.18.

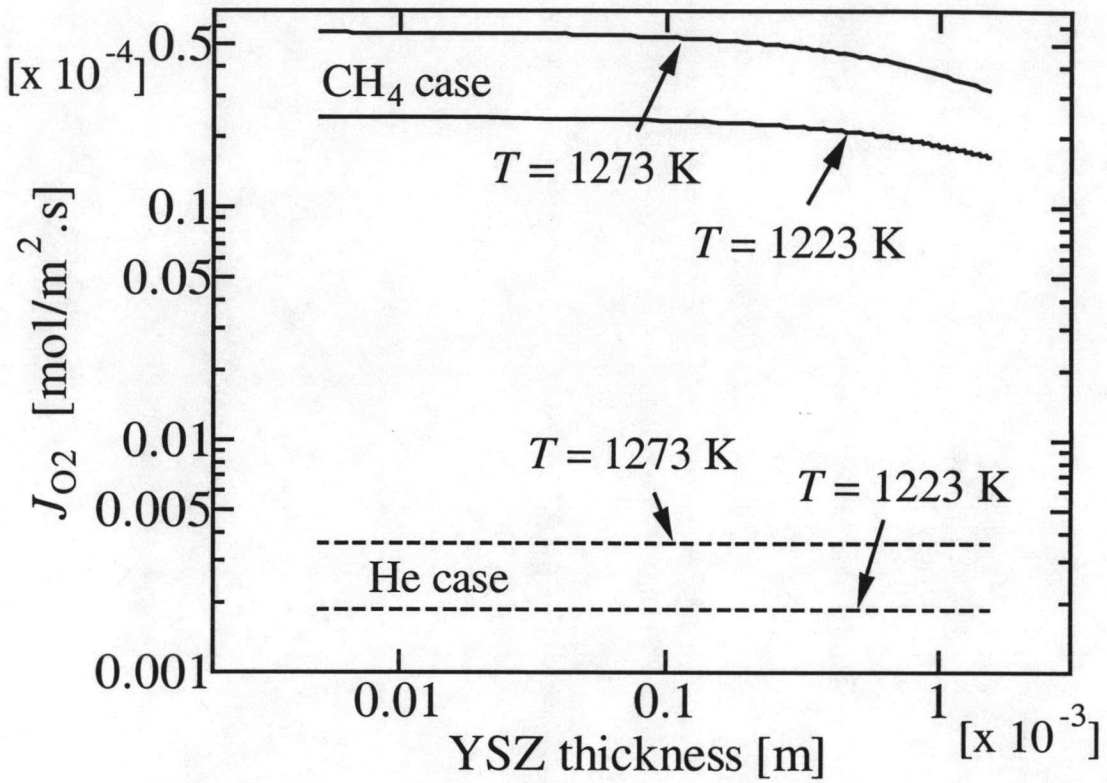

Figure 5.18 Effect of YSZ thickness on oxygen permeation in helium and methane case.

In the case of helium feed, the oxygen permeation flux is independent on the YSZ thickness as noted in the previous section that LaAlO is the rate-limiting step. However, in the case of methane feed, the resistance of YSZ electrolyte is comparable to that of LaAlO. The rate of oxygen permeation depends on YSZ electrolyte. The flux increases with decreasing the thickness of YSZ electrolyte membrane. However, for YSZ with thickness below 10 μm, there is no significant improvement on the oxygen flux. The tendency is the same for T = 1223 K and 1273 K.

5.2.5 Estimation of oxygen permeation from a model proposed by Han *et al.* (1997)

Han *et al.* (1997) proposed Eqs. (5.2)-(5.4) for the permeation of oxygen through YSZ membrane but their system was tested under unusual conditions; i.e. very thin YSZ membrane of 2-15μm, low oxygen partial pressure in an oxygen source chamber of 5.33 kPa and without external circuit (open circuit). Dashed lines in Figures 5.14 and 5.16 show the oxygen permeation flux calculated from Eqs. (5.2)-(5.4) using a YSZ with thickness of 1.5 mm. The estimated oxygen flux is much larger than that of the helium feed (compared with $V_{Per} = 0$ in Figure 5.14) and far less than that of the methane feed (compared with $V_{Per} = 0$ in Figure 5.16). This tendency can be understood by considering that the sweep gas of the permeate side contained 1% of hydrogen in their experiments (Han *et al.*, 1997).

Hydrogen in the sweep gas caused the promotion of the oxygen permeation by the surface reaction but the partial pressure was too low to complete the enhancement of the oxygen permeation. When hydrogen was mixed in the sweep gas, an electromotive force of about 1 V should be generated between the two electrodes. This may be the reason of the agreement with the plot of $V_{Per} = 1$ V in Figure 5.14.

The differences in the activation energy should be caused by the differences in the surface reaction on the anode material. Further studies are required to find more details.

All these results show that is essential for the model of SOFC type reactor to include the permeation of oxygen though the cathode, the electrolyte and the anode.

5.3 Modelling of SOFC reactor

By assuming plug flow and isothermal condition, the mass balance equation in the anode side (tube side) is given as

$$\frac{d\gamma_{t,i}}{dx} = \left\{ r_{t,i} + \left(\frac{S}{W}\right) J_i \right\} \left(\frac{W}{F_{t,T0}} \right) \qquad (5.18)$$

where the permeation rate of component i except for oxygen is zero ($J_i = 0$) because the YSZ electrolyte allows only oxygen to permeate.

At the entrance ($x = 0$), $\gamma_{t,CH_4} = \frac{F_{t,CH_4 0}}{F_{t,T0}}$, $\gamma_{t,i} = 0$ (products)

The mass balance equation in the cathode side (shell side) is given as

$$\frac{d\gamma_{s,i}}{dx} = \left\{ r_{s,i} - \left(\frac{S}{V}\right) J_i \right\} \left(\frac{V}{F_{s,T0}} \right) \qquad (5.19)$$

where $r_{s,i}$ is zero ($r_{s,i} = 0$) because oxygen or air was only passed through the cathode and permeate through the anode side, no reaction occurred on the cathode side.

At the entrance ($x = 0$), $\gamma_{s,O_2} = 1$ and 0.21 for pure oxygen and air feed, respectively.

The partial pressures in the tube side and the shell side can be determined as follows.

$$P_{t,i} = \frac{P_{t,T} \cdot \gamma_{t,i}}{\sum \gamma_{t,i}} \qquad (5.20)$$

$$P_{s,i} = \frac{P_{s,T} \cdot \gamma_{s,i}}{\sum \gamma_{s,i}} \qquad (5.21)$$

It should be noted that since the radiation is a very efficient for heat transfer due to high temperature as 1073-1273 K in the oven of our system, the temperature is uniform. The isothermal behavior of SOFC has already been reported in the literature (Costamagna *et al.*, 1998, 2004). Therefore, the simulations are considered isothermal and the energy balances are not included in this work.

The oxygen permeation rate through LSM/YSZ/LaAlO solid oxide fuel cell type reactor can be estimated from the permeation model in previous work (Section 5.2)

In the previous work, Tagawa *et al.*(1999) had been studied TPD on LaAlO powder. It was proposed that the oxygen species desorbed at low temperature (below 1000 K) were active for CO and CO_2 formation (oxygenate site) while the oxygen species desorbed at higher temperature (above 1000 K) were active for OCM to C2-hydrocarbon (coupling site). From the fuel cell type temperature-programmed desorption (FC-TPD) measurements in the previous section, the fraction of oxygen species for oxygenate site and coupling site were estimated by integration of oxygen FC-TPD results operated in closed circuit mode (as shown in Figure 5.6). The oxygen permeation rate was divided into two different types of oxygen species; i.e., oxygenate and coupling oxygen, by using mole fraction of oxygen species as shown below.

$$y_{O_2,oxy} = -2.381x10^{-3}T + 3.2661 \qquad (5.22)$$

$$J_{O_2,oxy} = y_{O_2,oxy} J_{O_2} \qquad (5.23)$$

$$J_{O_2,cou} = y_{O_2,cou} J_{O_2} = (1 - y_{O_2,oxy}) J_{O_2} \qquad (5.24)$$

Eq. (5.21) was determined from FC-TPD experimental results in Figure 5.6.

When methane was fed on the anode and oxygen was permeated from the cathode to the anode side, the following oxidation reactions were proceeded.

$$2CH_4 + 1/2O_2 \rightarrow C_2H_6 + H_2O \quad (5.25)$$

$$C_2H_6 + 1/2O_2 \rightarrow C_2H_4 + H_2O \quad (5.26)$$

$$CH_4 + 3/2O_2 \rightarrow CO + 2H_2O \quad (5.27)$$

$$CH_4 + 2O_2 \rightarrow CO_2 + 2H_2O \quad (5.28)$$

$$C_2H_6 + 7/2O_2 \rightarrow 2CO_2 + 3H_2O \quad (5.29)$$

Assuming the first order kinetics with respect to surface concentration of methane and oxygen, the rate equation for the product i can be expressed as follows.

$$r_i = k_i' \varphi_{CH_4} \varphi_{O_2,j} \quad (5.30)$$

The surface concentration of methane (φ_{CH_4}) was supposed to have linear relationship with P_{CH_4} as follows.

$$\varphi_{CH_4} \propto P_{CH_4} \quad (5.31)$$

In the previous study on FC-TPD of oxygen (Section 5.1), an important role of oxygen desorption from anode material has been pointed out. The activation energy of surface oxygen desorption (open circuit) and that of oxygen permeation (closed circuit) agreed with each other in both cases of oxygenate oxygen and coupling oxygen. These results suggested the permeation of oxygen strongly depended on the surface oxygen species. Thus linear relationship between surface concentration of oxygen ($\varphi_{O_2,j}$) and

oxygen flux ($J_{O_2,j}$) was also supposed as follows.

$$\varphi_{O_2,j} \propto J_{O_2,j} \tag{5.32}$$

Where j represents either coupling oxygen (cou) or oxygenate oxygen (oxy).

Then, the kinetic rate expressions determined for each of the above reactions are given as follows.

$$r_1 = k_1 P_{CH_4} J_{O_2,cou} \tag{5.33}$$

$$r_2 = k_2 P_{C_2H_6} J_{O_2,cou} \tag{5.34}$$

$$r_3 = k_3 P_{CH_4} J_{O_2,oxy} \tag{5.35}$$

$$r_4 = k_4 P_{CH_4} J_{O_2,oxy} \tag{5.36}$$

$$r_5 = k_5 P_{C_2H_6} J_{O_2,oxy} \tag{5.37}$$

Therefore, the reaction rate of component i can be expressed by stoichiometric relations as follows:

$$r_{CH_4} = -2r_1 - r_3 - r_4 \tag{5.38}$$

$$r_{C_2H_6} = r_1 - r_2 - r_5 \tag{5.39}$$

$$r_{C_2H_4} = r_2 \tag{5.40}$$

$$r_{CO} = r_3 \tag{5.41}$$

$$r_{CO_2} = r_4 + r_5 \tag{5.42}$$

$$r_{O_2} = -\tfrac{1}{2} r_1 - \tfrac{1}{2} r_2 - \tfrac{3}{2} r_3 - 2r_4 - \tfrac{7}{2} r_5 \tag{5.43}$$

5.3.1 Selection of an optimum mist solution concentration for the anode preparation

Figure 5.19 shows the effect of the mist solution concentration on methane conversion (filled symbols) and C2 selectivity (open symbols).

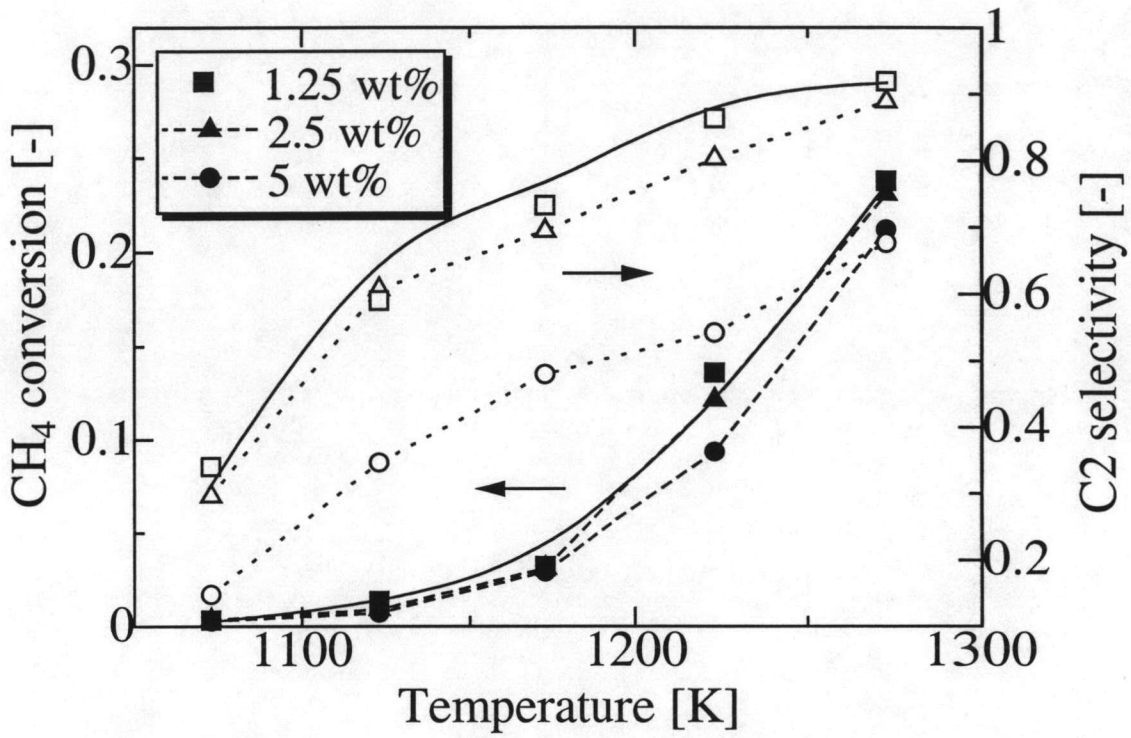

Figure 5.19 Effect of temperature on methane conversion and C2 selectivity at difference anode preparation; $F_{CH_4,0} = 3.4 \times 10^{-6}$ mol s^{-1}, $W = 4.0 \times 10^{-5}$ kg, pure oxygen feed on the cathode.

SOFC reactor was operated in a closed circuit mode without external resistance (short circuit, $R_L = 0$). C2 selectivity increased with decreasing concentration of the mist solution or with increasing reaction temperature. The solid lines represent calculated results, which will be described later. At lower concentration of the mist solution, particles with smaller sizes were obtained. The small particle sizes are effective for C2 product formation (Moe *et al.*, 1998a). As the mist solution

concentration of 1.25 wt% showed the highest selectivity, it was chosen as an optimum concentration for the following studies. With the optimum anode preparation condition, the conversion and C2 selectivity were 23.7 % and 91.7 %, respectively, at 1273 K.

It should be noted that carbon deposition on the anode is a typical phenomenon taking place in solid oxide fuel cells with hydrocarbon feed. However, all experimental results in this study were recorded at steady-state conditions and the carbon balance was checked and found to be within 99.8%. In case of a possible carbon deposition, the cell was treated by feeding pure oxygen (1.02×10^{-5} mol s^{-1}) to the anode side, before running each set of experiments. The temperature was raised to 773 and 1223 K with a holding time of 6 h for each step.

5.3.2 Permeation of oxygen

The amount of oxygen permeation is very important for selective oxidations. For a non-porous solid electrolyte, it can be related to current density as described by Faraday's law as follows.

$$I = J_{O_2} \cdot 4F \qquad (5.44)$$

The current density can be directly converted to current by multiply with the effective area.

Figure 5.20 shows the effect of temperature on the current. Three kinds of current were plotted as follows: 1) current recorded from the current meter, 2) equivalent current calculated from the oxygen consumption from product distribution and 3) equivalent current estimated from the permeation model. Due to no oxygen in gas phase was detected from the anode exit gas; the permeated oxygen was all consumed in the reactions with methane.

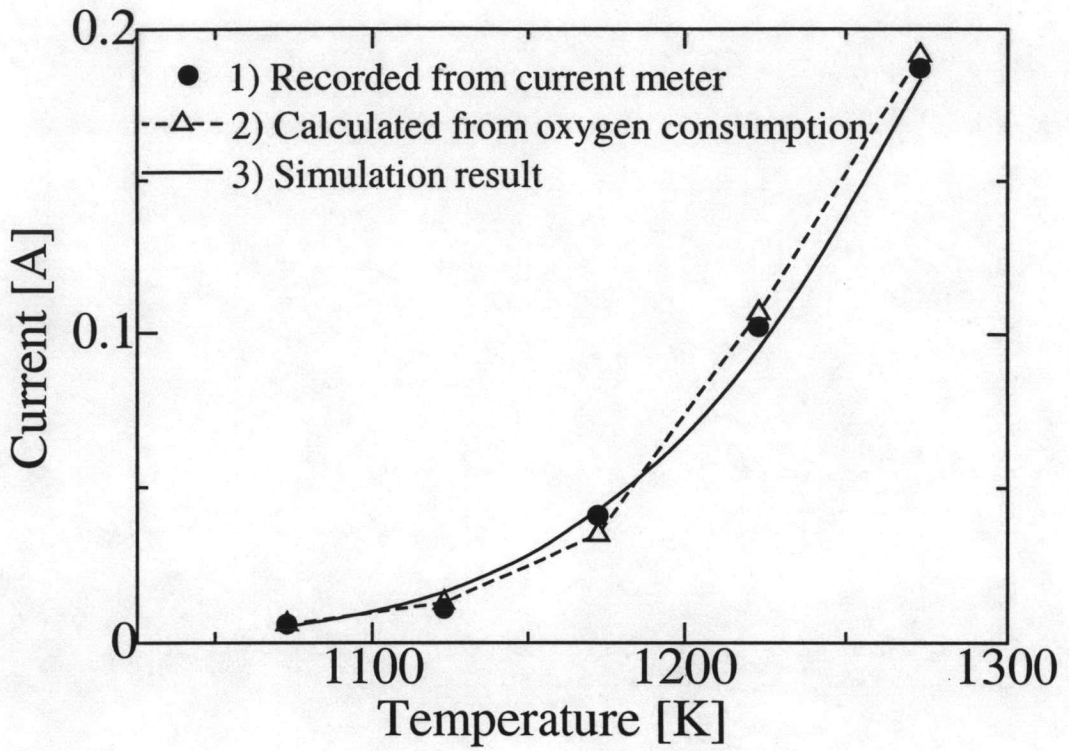

Figure 5.20 Effect of temperature on current with short circuit mode; $F_{CH_4,0} = 6.8 \times 10^{-6}$ mol s^{-1}, $W = 4.0 \times 10^{-5}$ kg, pure oxygen feed on the cathode.

As shown in Figure 5.20, the current values predicted from our model agreed well with those of experimental values from the current meter as well as those from the product distribution. These agreements indicated that the amount of reacted oxygen species (J_{O_2}) could be calculated from the permeation model and that the electrolyte used in the study was pin-hole free. Then, J_{O_2} was calculated with our permeation model for Section 5.3.3.

5.3.3 Reactor performance (short circuit, $R_L = 0$)

SOFC reactor was operated in the closed circuit mode without external resistance (short circuit, $R_L = 0$). The kinetic rate expressions were determined for each of the above reaction by fitting the experimental data shown in Figure 5.21.

$$k_1 = 3.70\text{x}10^7 \exp\left(\frac{-215000}{R_g T}\right) \quad (5.45)$$

$$k_2 = 2.96\text{x}10^5 \exp\left(\frac{-110000}{R_g T}\right) \quad (5.46)$$

$$k_3 = 4.14\text{x}10^3 \exp\left(\frac{-124000}{R_g T}\right) \quad (5.47)$$

$$k_4 = 2.96\text{x}10^3 \exp\left(\frac{-131000}{R_g T}\right) \quad (5.48)$$

$$k_5 = 1.78\text{x}10^5 \exp\left(\frac{-120000}{R_g T}\right) \quad (5.49)$$

Figure 5.21 shows the reactor performance for the case with air feed on the cathode. Figure 5.21-(a) shows the effect of temperature on methane conversion and C2 selectivity along with calculated results. The conversion and C2 selectivity increased with increasing temperature. These follow the same trend for the case with pure oxygen feed on the cathode; however, lower conversion was achieved. Figure 5.21-(b) shows the selectivity of each product under the same conditions. It is worth noting that the selectivity of CO and CO_2 decreases with increasing temperature. The solid lines in Figures 5.19 and 5.21 represent calculated results which were carried out as follows: J_{O_2} was estimated from the model. The oxygen permeation rate was divided into two different types of oxygen species; i.e., oxygenate and coupling oxygen, by using mole

fraction of oxygen species as shown in Eqs. (5.22)-(5.24).

Then C_2H_4 and C_2H_6 formations which use the oxygen species for coupling ($O_{2,\,cou}$) were calculated by using Eqs. (5.33) and (5.34). CO and CO_2 formation which using the oxygen species for oxygenate ($O_{2,\,oxy}$) were calculated by using Eqs. (5.35)-(5.37). Methane conversion and product selectivity were calculated by using Eqs. (5.18) and (5.20). The calculated results (solid lines) agreed well with the experimental results. The maximum C2 yield of 16.8 % was obtained at 1273 K in case of air feed at cathode side by multiply the conversion and the selectivity shown in Figure 5.21-(a), where C2 yield of 21.7% was obtained in case of pure oxygen feed shown in Figure 5.19.

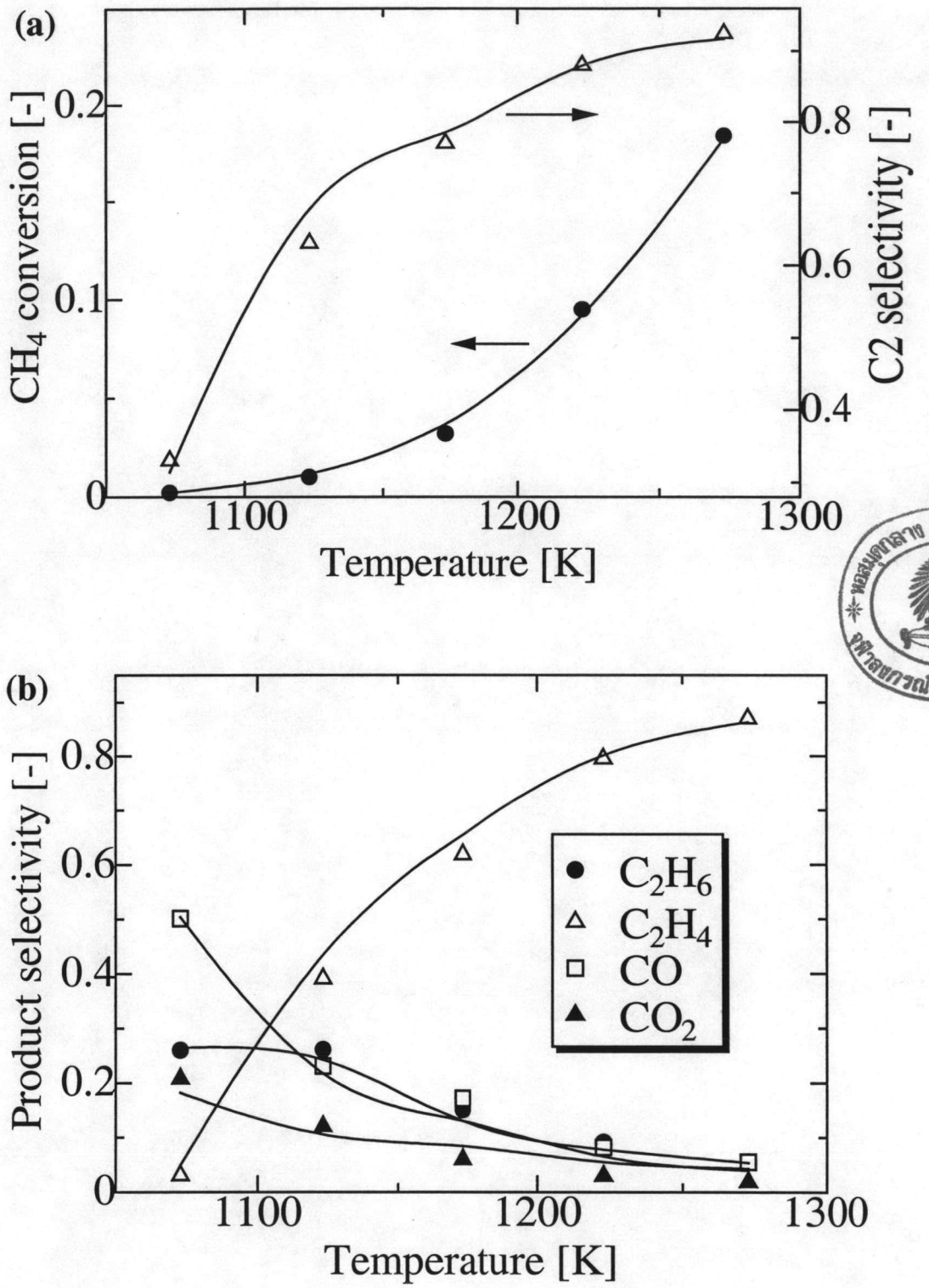

Figure 5.21 Effect of temperature (a) on methane conversion and C2 selectivity, and (b) on the product selectivity distribution; $F_{CH_4,0} = 3.4 \times 10^{-6}$ mol s^{-1}, $W = 4.0 \times 10^{-5}$ kg, air feed on the cathode.

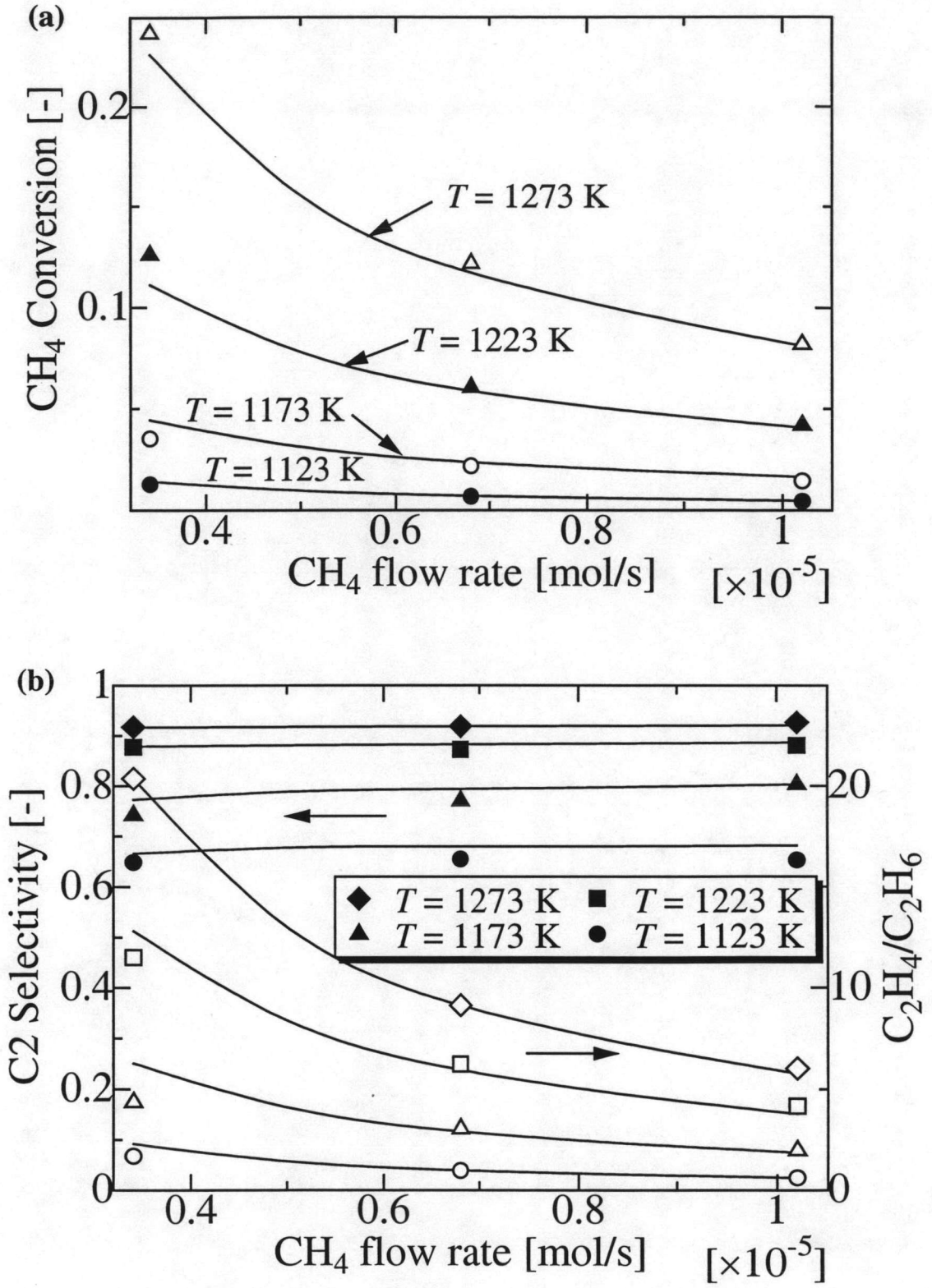

Figure 5.22 Effect of methane flow rate (a) on methane conversion and (b) on C2 selectivity and C_2H_4/C_2H_6 ratio at various temperatures; $W = 4.0 \times 10^{-5}$ kg, pure oxygen feed on the cathode.

Effects of methane flow rate on methane conversion and C2 selectivity are shown in Figure 5.22. The calculated results in Figure 5.22 followed the same calculation method as used in Figure 5.21. As shown in Figure 5.22-(a), the methane conversion increases with decreasing methane flow rate, which is in good agreement with the calculated values (solid lines).

As shown in Figure 5.22-(b), the C2 selectivity is almost independent of methane flow rate. This suggests that oxygenate products and coupling products are formed in a parallel manner. On the other hand, C_2H_4/C_2H_6 ratio decreases with increasing methane flow rate. Because of shorter residence time, consecutive ethylene production from ethane decreases with increasing methane flow rate. Our developed model can predict the experimental results very well.

It should be noted that Guo *et al.* (1999) proposed the complex kinetic expressions to explain complicated changes in selectivity while this study proposed the simple kinetics by assuming two kinds of oxygen species with different activity.

5.3.4 Chemicals-energy cogeneration with SOFC reactor (closed circuit with external load, R_L)

A simplified short circuit model is shown in Figure 5.23-(a). In normal fuel cell operation, an external load is connected to the cell for power utilization. A simplified series circuit model is proposed in Figure 5.23-(b). The internal resistance of cell can be determined from the maximum power transfer theorem (Siskind, 1965) as described below. Figure 5.23-(b) consists of a voltage source (SOFC reactor unit) with a variable external load resistor (R_L).

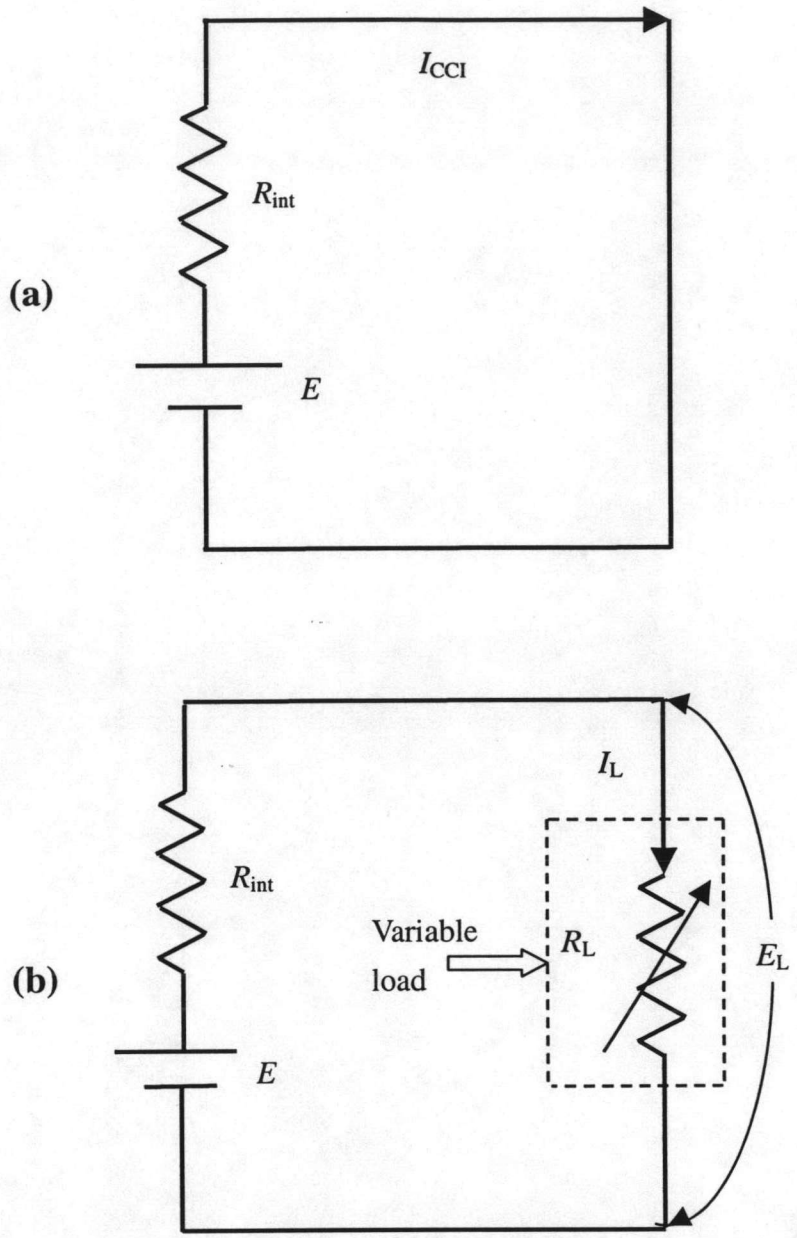

Figure 5.23 Simplified circuit diagram to illustrate SOFC reactor

(a) Operation with short circuit mode

(b) Operation with an external variable load resistor.

If $R_L = \infty$ (open circuit), current $I_L = 0$ and power at load, $P_L = 0$; also, if $R_L = 0$ (short circuit), voltage $E_L = 0$ and $P_L = 0$. When R_L is neither ∞ or 0, P_L is not 0. A maximum power transferred to the load occurs when $R_L = R_{int}$. R_{int} is the overall resistance including ohmic, activation and concentration polarization resistances inside

the cell unit. Therefore, R_{int} value varies with operating conditions such as temperature, $P_{O_2,CA}$, P_{CH_4} and should be experimentally estimated.

Figure 5.24 shows the load resistance-voltage and load resistance-power plots at various temperatures in case of (a) oxygen and (b) air feed on the cathode. The open circuit voltages are in range of 1.02-1.08 V, which is nearly equal to the theoretical value of the C_2H_4 formation from C_2H_6 (Tagawa *et al.*, 1999). Power increases with increasing temperature. With increasing the operating temperature, the chemical reaction can be enhanced as well as oxygen permeability through the YSZ. It should be noted that when the current-voltage is plotted for both cases as shown in Figure 5.25, a linear decrease of voltage with current is observed, indicating that the over-potential is mainly governed by the ohmic resistance of the cell.

Comparing between Figure 5.24-(a) and Figure 5.24-(b), changing oxygen to air feed on the cathode, the power decreases due to decreasing the driving force of oxygen gradient. However using air instead of oxygen can be competitive from a viewpoint of the oxygen purification cost.

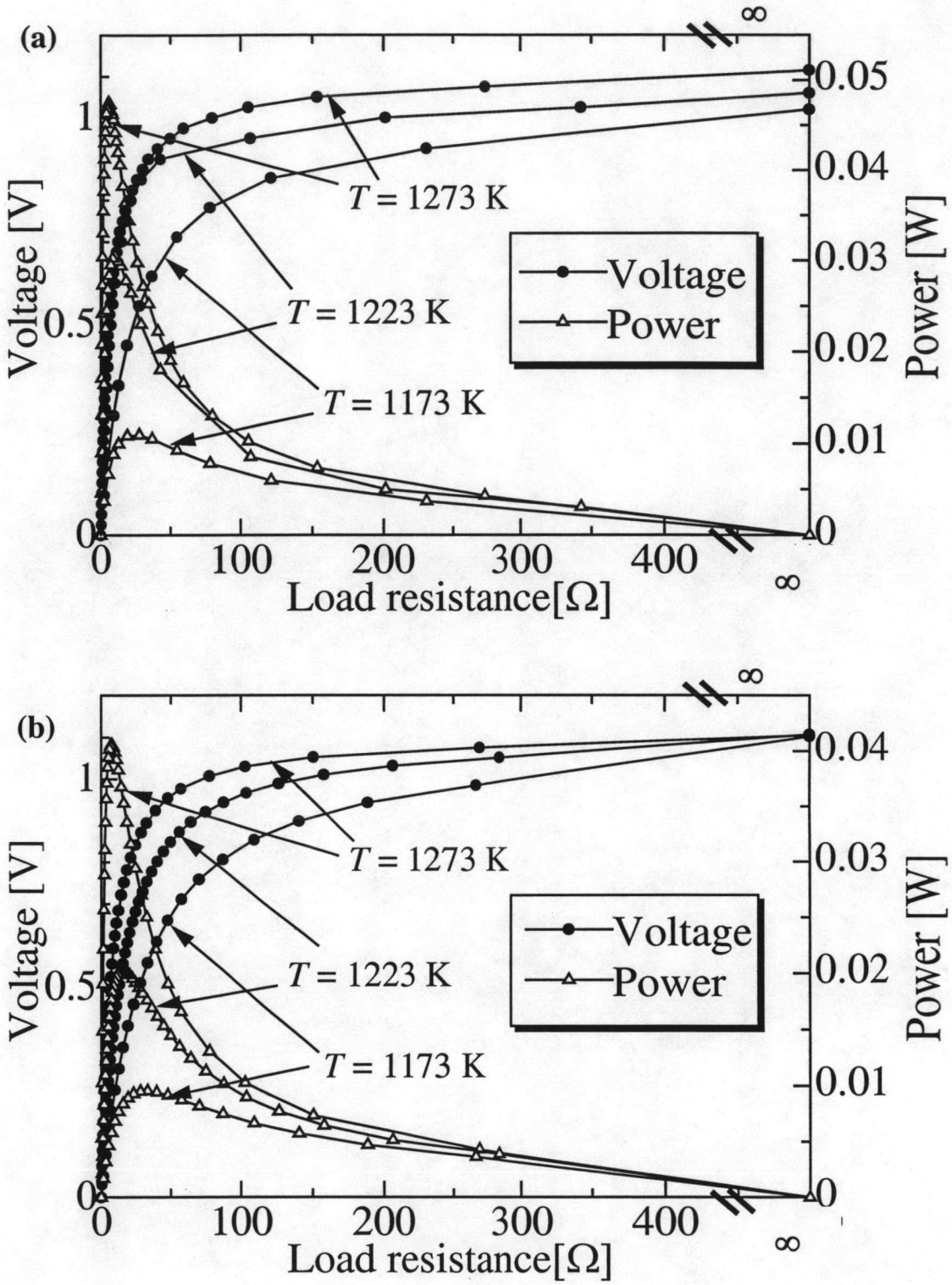

Figure 5.24 Load resistance-voltage and load resistance-power at various temperatures in the case of (a) pure oxygen feed on the cathode and (b) air feed on the cathode; $F_{CH_4,0} = 6.8 \times 10^{-6}$ mol s^{-1}, $W = 4.0 \times 10^{-5}$ kg.

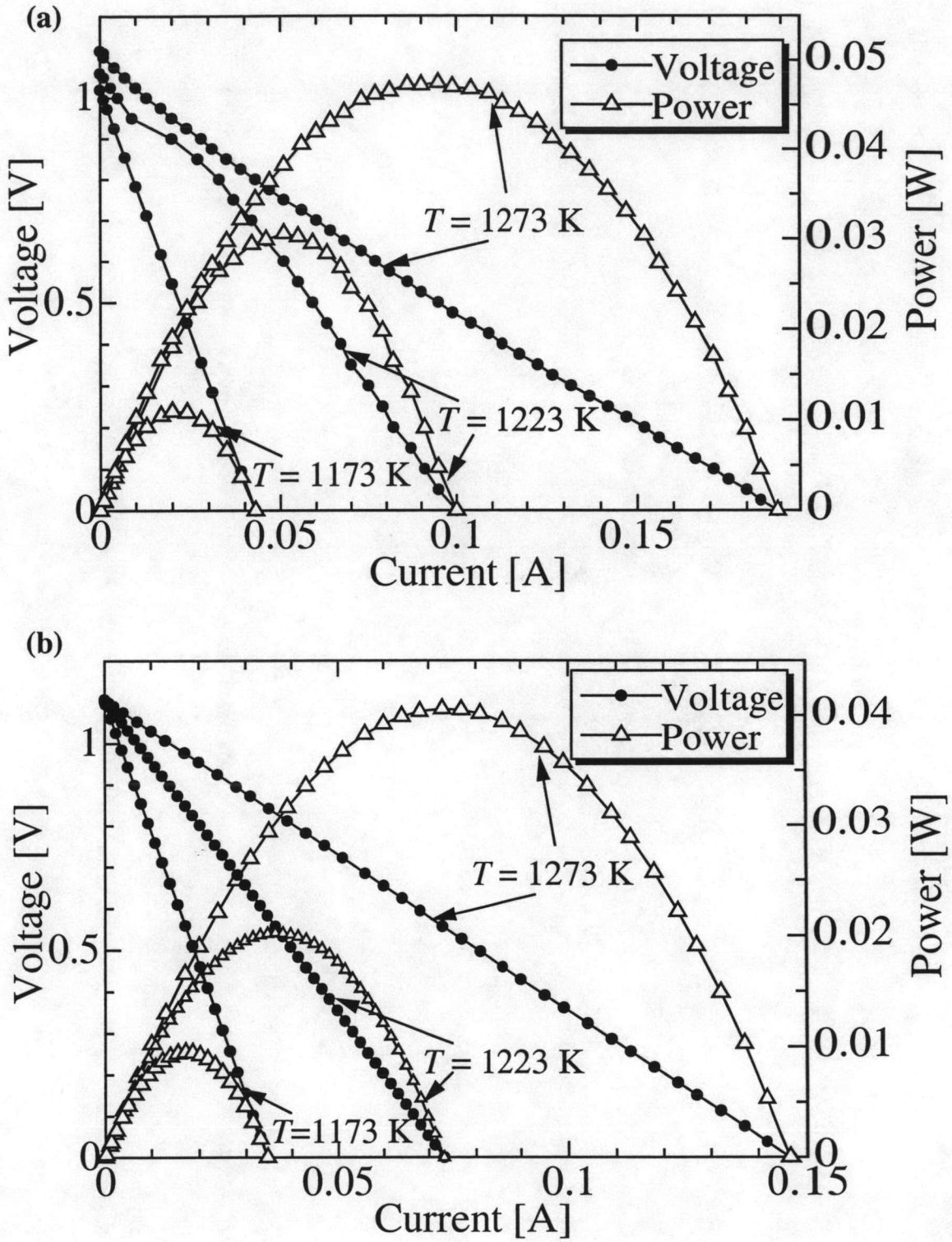

Figure 5.25 Current-voltage and current-power at various temperatures in the case of (a) pure oxygen feed on the cathode and (b) air feed on the cathode; $F_{CH_4,O} = 6.8 \times 10^{-6}$ mol s^{-1}, $W = 4.0 \times 10^{-5}$ kg.

Figure 5.26 shows the relation of internal cell resistance (R_{int}) and temperature. The effect of oxygen partial pressure on R_{int} was studied by using pure oxygen and air. Even though pure methane was used in every experiment, the methane conversion which effect to methane partial pressure was taken into account. Methane and oxygen partial pressure can be calculated from Eqs.(5.20) and (5.21), respectively. The following expressions can be obtained.

$$R_{int} = \frac{0.0567}{P_{O_2,CA}^{0.2} P_{CH_4}^{0.51} T} \exp\left(\frac{166000}{R_g T}\right) \tag{5.50}$$

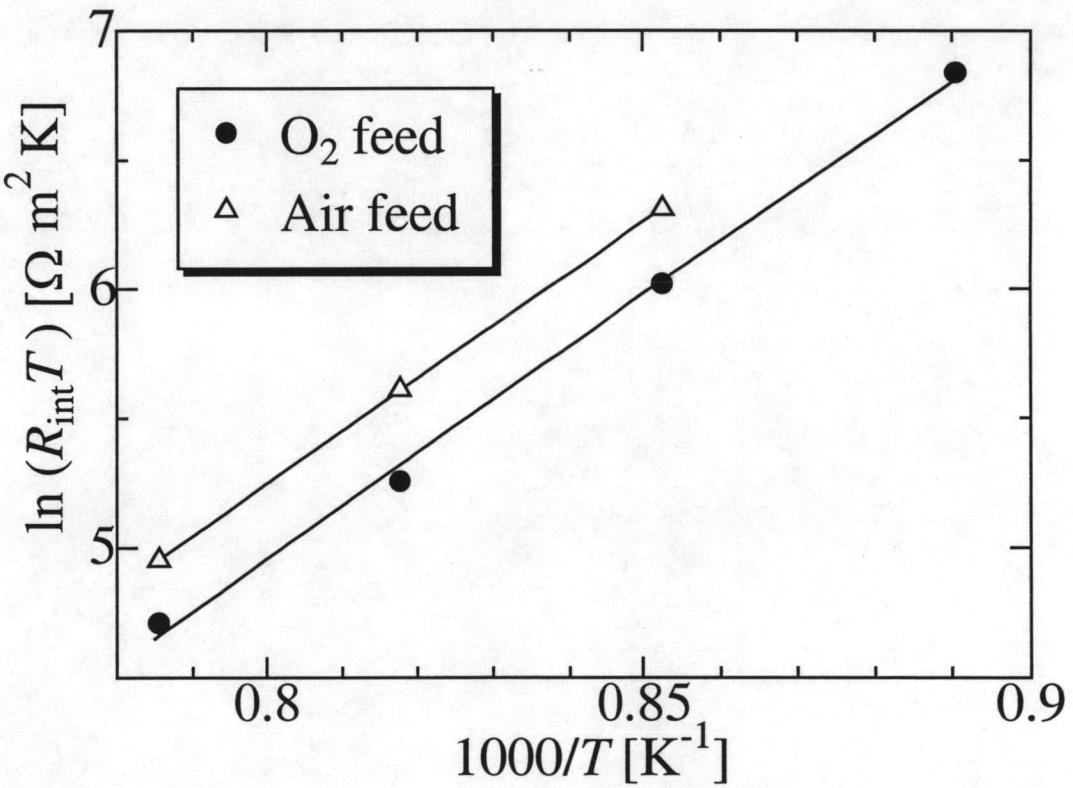

Figure 5.26 Arrhenius' plot between ln ($R_{int}T$) and 1000/T .

These results show that higher $P_{O_2,CA}$ and P_{CH_4} or operating at higher temperature gives lower R_{int}.

Figure 5.27-(a) shows the relationship between load resistance and methane conversion. In the case of external load, the current can be calculated from

$$I_L = \frac{E}{R_{int} + R_L} \qquad (5.51)$$

Then, the calculated current was used to estimate the oxygen permeated flux to anode by Eq. (5.44).

The filled symbol represents pure oxygen feed on the cathode case while the open symbol represents air feed on the cathode case. The solid line represents calculated results. I was estimated from R_L value with Eqs. (5.50) and (5.51) using E values shown as a voltage in Figure 5.24 for oxygen and air feed on the cathode. Using mole fraction of oxygen species shown in Eq. (5.22) and Eqs. (5.23) and (5.24), the amount of oxygen for oxygenate and coupling site were estimated, respectively. Then C_2H_4 and C_2H_6 formation were calculated by using Eqs. (5.33) and (5.34), while CO and CO_2 formation were calculated by using Eqs. (5.35)-(5.37) as described in the previous section. Methane conversion was calculated by using Eqs. (5.18) and (5.20). The calculated results are shown in Figure 5.27-(a) as solid lines. With increasing load resistance, oxygen hardly permeated due to increasing electron transfer resistance. This resulted in decrease of methane conversion. Changing oxygen to air feed on the cathode, the methane conversion decreased due to decreasing the amount of permeated oxygen.

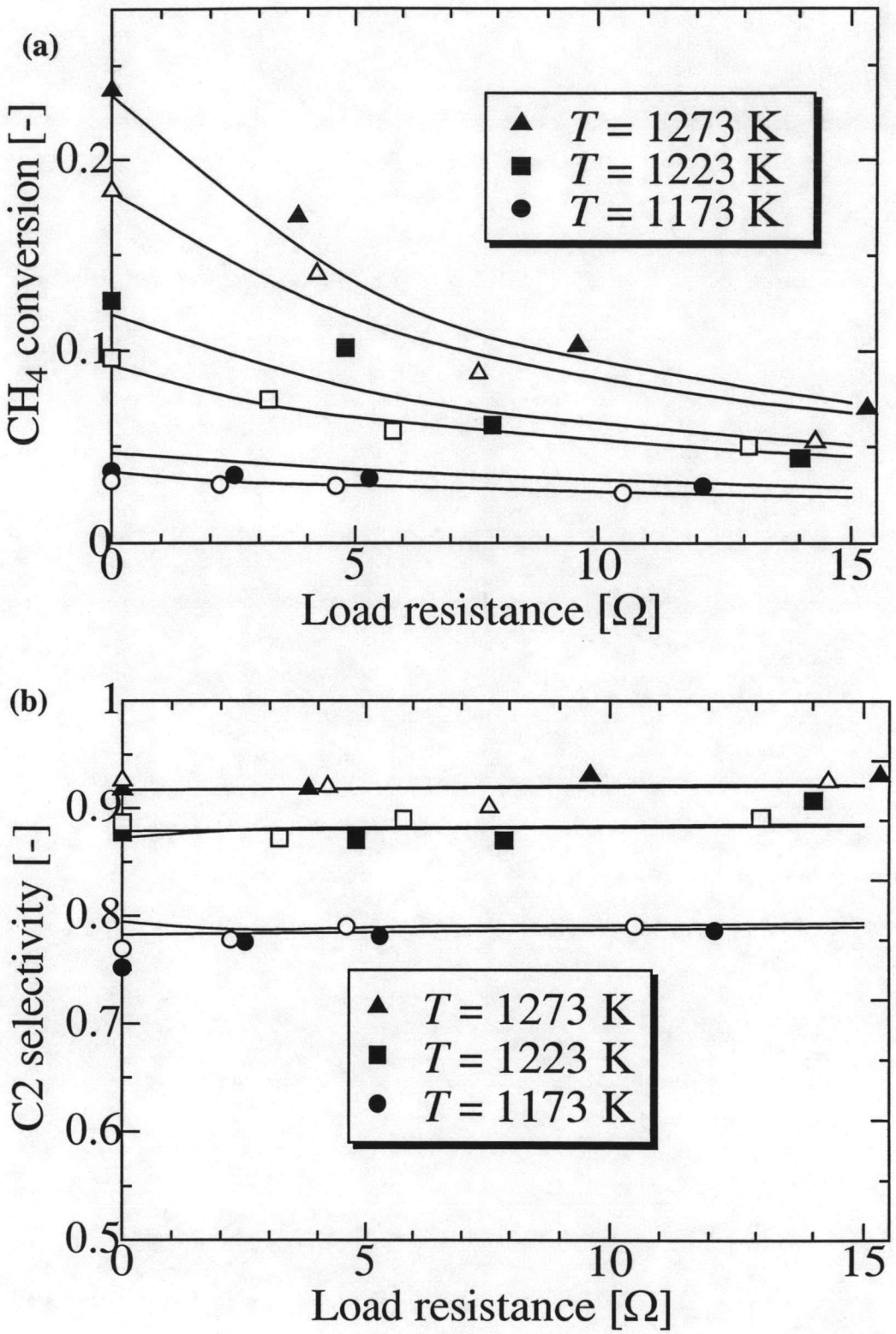

Figure 5.27 Effect of load resistance (a) on methane conversion and (b) on C2 selectivity at various temperatures; $F_{CH_4,0}$ = 3.4x10^{-6} mol s^{-1}, W = 4.0x10^{-5} kg, filled symbol = pure oxygen feed on the cathode, open symbol = air feed on the cathode.

Figure 5.27-(b) shows the relationship between R_L and the selectivity. Load resistance showed insignificantly effect on C2 selectivity while operating temperature showed strong effect. The selectivity was calculated by the same method mentioned above. Changing oxygen to air feed on the cathode, C2 selectivity was insignificantly affected. The calculated results agreed well with the experimental results.

5.4 Simulation of SOFC reactor operating at maximum power transfer

From a simplified short circuit model as shown in Figure 5.23-(a). The closed circuit current density (I_{CCI}) can be calculated from oxygen permeation model and using Eq. (5.41)

As shown in Figure 5.25, a linear decrease of voltage with current which tends the power and current relation to be parabolic was observed, indicating that the over-potential is mainly governed by the ohmic resistance of the cell. Assuming that cell is operated at maximum power at load which occurs when $R_L = R_{int}$ could be verified (Minh and Takahashi, 1995). Then the corresponding current density (I_L) and voltage across the load (E_L) are estimated as follows (Siskind, 1965).

$$I_L = \frac{I_{CCI}}{2} \qquad (5.52)$$

$$E_L = \frac{E}{2} = I_L R_L \qquad (5.53)$$

Then the power at load operated at the maximum power transfer is

$$P_L = (I_L \text{ x } S) \text{ x } E_L \qquad (5.54)$$

The values of overall efficiency can be based on heat of reaction of methane combustion ($-\Delta H_{CO_2}$) (Goto *et al.*, 2003) and on that of the selective coupling to ethylene ($-\Delta H_{C_2H_4}$) as follows;

$$CH_4 + 2O_2 \rightarrow CO_2 + 2H_2O \qquad (5.55)$$

$(-\Delta H_{CO_2})$ at operating temperature T =

$$-802600+15.884(T-T_{st})-1.698\text{x}10^{-2}\left(\frac{T^2-T_{st}^2}{2}\right)-1.227\text{x}10^{-5}\left(\frac{T^3-T_{st}^3}{3}\right)$$

$$+8.660\text{x}10^{-9}\left(\frac{T^4-T_{st}^4}{4}\right) \qquad (5.56)$$

where T_{st} is standard temperature (298 K)

$$CH_4 + 1/2O_2 \rightarrow 1/2C_2H_4 + H_2O \qquad (5.57)$$

$(-\Delta H_{C_2H_4})$ at operating temperature T =

$$-141050+1.588(T-T_{st})+2.226\text{x}10^{-2}\left(\frac{T^2-T_{st}^2}{2}\right)-4.025\text{x}10^{-5}\left(\frac{T^3-T_{st}^3}{3}\right)$$

$$+1.558\text{x}10^{-8}\left(\frac{T^4-T_{st}^4}{4}\right) \qquad (5.58)$$

The definition of the overall efficiency is defined as follows.

$$\eta_{OV,k}=\frac{P_T}{(-\Delta H_k)F_{CH_4,0}};k=CO_2,C_2H_4 \qquad (5.59)$$

5.4.1 Comparison between simulation and experimental results

The mathematical model was verified by comparing simulation results with the experimental results. EQUATRAN-G (Omega Simulation, Japan), all-purpose equation solver, was employed to solve the equations. Table 5.7 shows the current (I_L x S), voltage (E_L) and power (P_L) obtained from the experiments and simulations when the cell is operated at maximum power at load. The voltage and current at maximum power for the cases of pure oxygen and air feeds on the cathode are obtained from Figure 5.25 in the previous section. Good agreements between simulation and experimental results are obtained.

Table 5.7 Comparison of current (I_L x S), voltage (E_L) and power (P_L) between experimental and simulation results ($F_{CH_4,0} = 6.8x10^{-6}$ mol s^{-1}, $W = 4.0x10^{-5}$ kg and operation at maximum power at load).

(a) In the case of pure oxygen feed on the cathode

Temperature [K]	Experiment (Simulation)*		
	(I_L x S) [A]	E_L [V]	P_L [W]
1173	0.020 (0.021)	0.546 (0.483)	0.011 (0.010)
1223	0.051 (0.047)	0.562 (0.512)	0.029 (0.024)
1273	0.095 (0.090)	0.500 (0.501)	0.048 (0.045)

(b) In the case of air feed on the cathode

Temperature [K]	Experiment (Simulation)*		
	(I_L x S) [A]	E_L [V]	P_L [W]
1173	0.017 (0.017)	0.559 (0.539)	0.010 (0.009)
1223	0.036 (0.038)	0.557 (0.550)	0.020 (0.021)
1273	0.073 (0.073)	0.556 (0.550)	0.041(0.040)

*** Parentheses show the simulation results**

5.4.2 Effect of operating temperature

Figure 5.28-(a) shows the effect of temperature on methane conversion and C2 selectivity in both cases of pure oxygen and air feeds on the cathode. The conversion and C2 selectivity increase with increasing temperature.

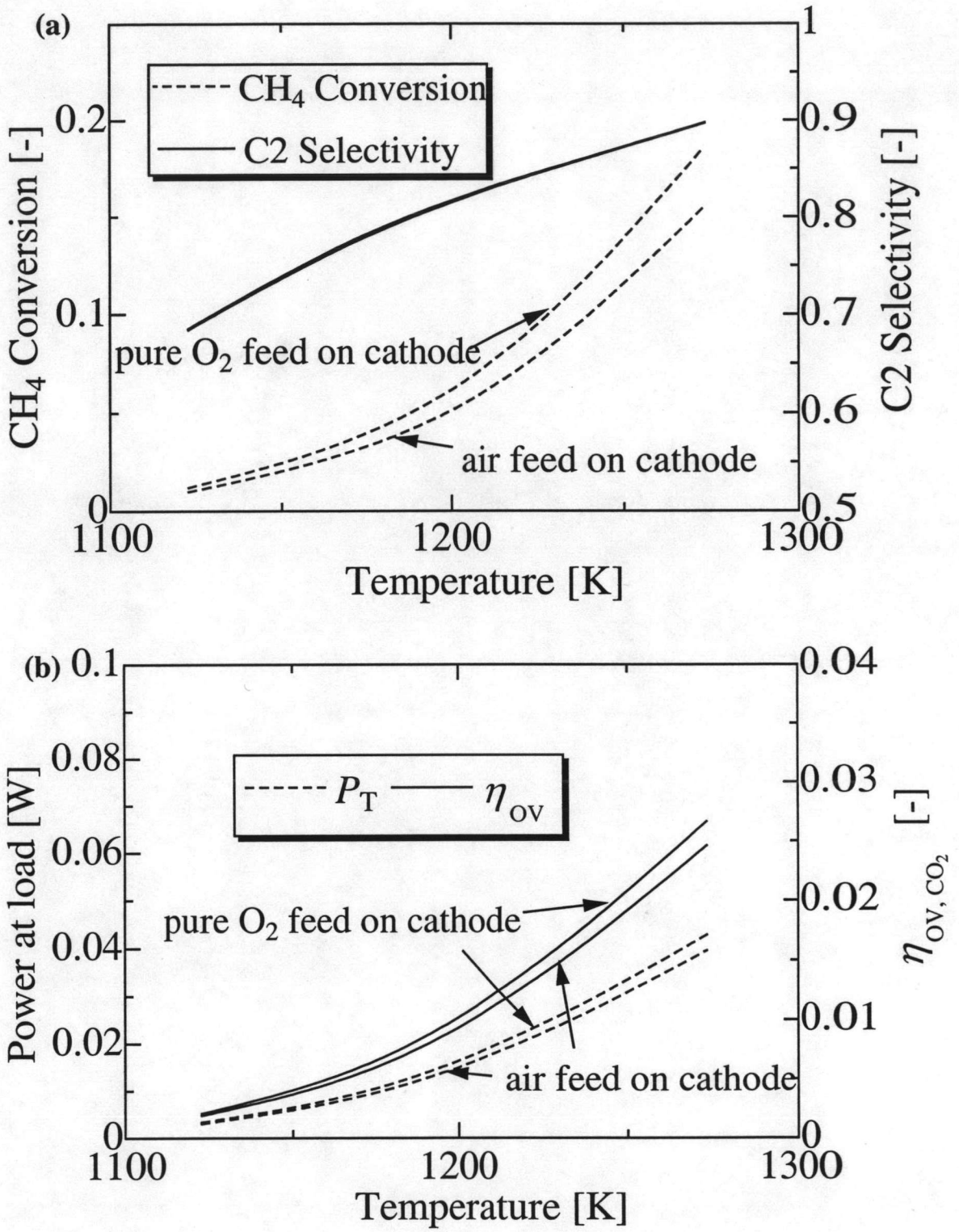

Figure 5.28 Effect of operating temperature on (a) methane conversion and C2 selectivity and (b) power at load and overall efficiency ($F_{CH_4,0}$ = 2.0x10^{-6} mol s^{-1}, W = 4.0x10^{-5} kg, $P_{s,T} = P_{t,T}$ = 1.013x10^{5} Pa, pure methane feed on the anode).

Slightly higher conversion is achieved in the case of pure oxygen feed on the cathode due to the increased driving force of oxygen partial pressure. However, the values of C2 selectivity are almost the same for both cases. Figure 5.28-(b) shows the effect of temperature on power at load and overall efficiency. They increase with increasing operating temperature due to the increased oxygen permeation rate. It should be noted that the overall efficiency is low because the calculation is based on the overall heat of combustion of methane to carbon dioxide. In addition, the differences in the power and the overall efficiency between the cases with air feed and pure oxygen feed are not significant, indicating that the effort to purify air to achieve high oxygen concentration is unnecessary.

5.4.3 Effect of feed flow rate and methane feed concentration

Figures 5.29 and 5.30 show the effect of feed flow rate on the reactor performances at various levels of methane feed concentration. Methane was diluted with inert gas and fed to the reactor. As shown in Figure 5.29, the methane conversion decreases with increasing total molar flow rate for all methane feed concentration due to the decreased residence time. In addition, C2 selectivity is only slightly decreased with decreasing total molar flow rate or increasing the inert mole fraction. It is because the oxygenate products and coupling products are mainly formed in a parallel manner. In our system, most of C2 production is ethylene, which is more favored than ethane.

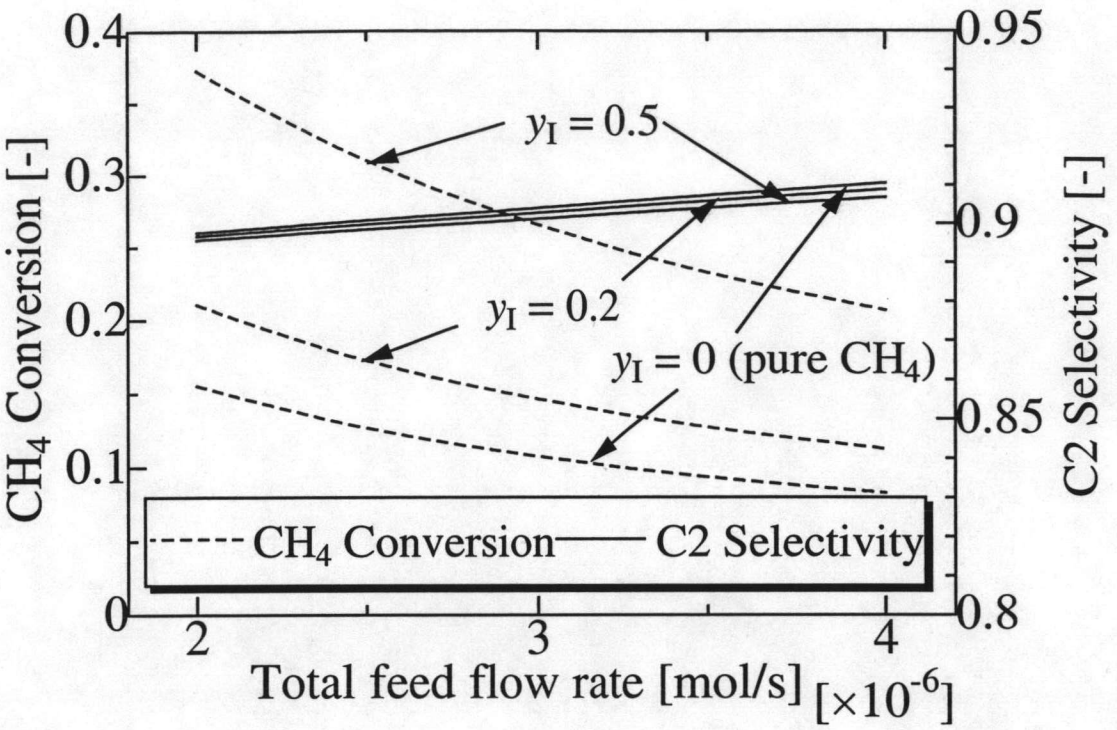

Figure 5.29 Effect of total feed flow rate on methane conversion and C2 selectivity at various methane feed concentration ($W = 4.0\text{x}10^{-5}$ kg, $P_{s,T} = P_{t,T} = 1.013\text{x}10^{5}$ Pa, $T =$ 1273 K, air feed on the cathode).

Power at load increases with increasing methane feed concentration while it slightly increases with increasing the total molar flow rate as shown in Figure 5.30. It is important to note that the power at load in case of dilution with inert gas is obviously lower than that with pure methane because the internal cell resistance is influenced by partial pressure of methane; i.e., it increases with the decrease of methane partial pressure. In addition, the current, which is corresponding to oxygen permeation, increases with increasing methane partial pressure. Figure 5.30 also provides the overall efficiency based on the heat of selective oxidation to ethylene. The value as high as 17% can be obtained. This value is corresponding to the overall efficiency based on the heat of combustion of 2.9%. It should be noted that it might be difficult to define the overall efficiency for this SOFC system because there are many reactions involved

whose corresponding maximum possible works are different. For example at T = 1273 K, the Gibbs' free energy of the methane conversion to carbon dioxide and to ethylene are 7.958×10^5 and 1.533×10^5 J mol^{-1}, respectively. The extent of undesired complete oxidation reaction can significantly increase the value of the overall efficiency based on the ethylene production.

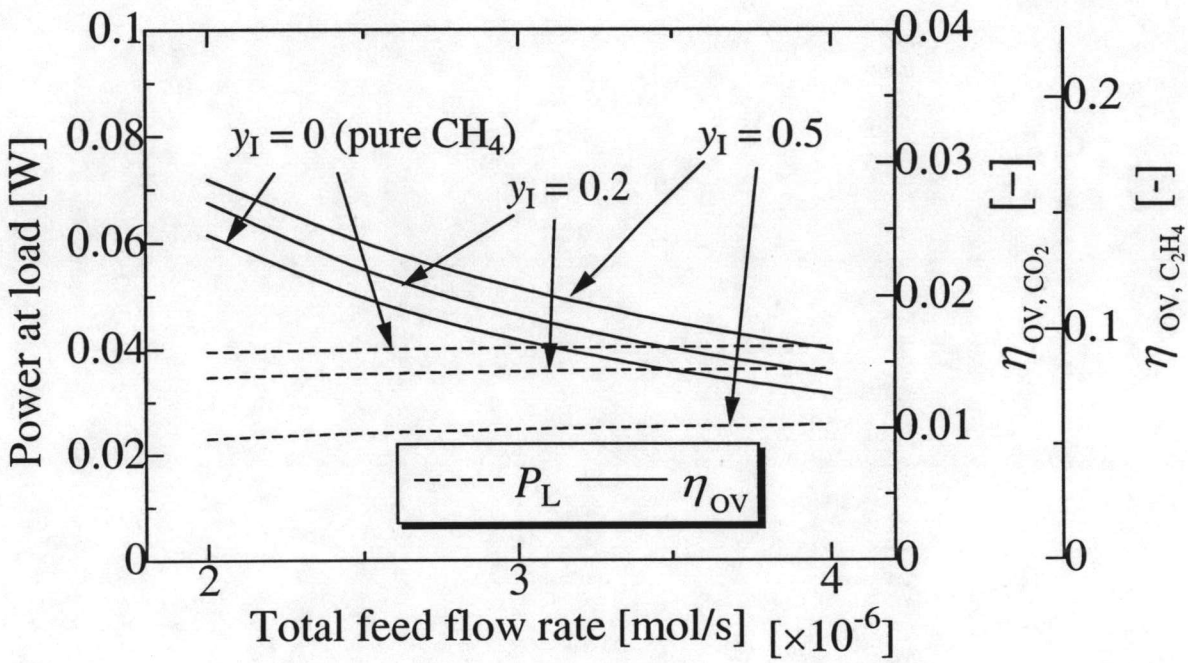

Figure 5.30 Effect of total feed flow rate on power at load and overall efficiency at various methane feed concentration ($W = 4.0 \times 10^{-5}$ kg, $P_{s,T} = P_{t,T} = 1.013 \times 10^5$ Pa, T = 1273 K, air feed on the cathode).

5.4.4 Effect of operating pressure

In order to avoid cell damages, the operating pressures in both sides of the cells are maintained at the same value. The results shown in Figure 5.31 indicate that the methane conversion increases with increasing operating pressure while C2 selectivity is insignificantly affected. Corresponding to the increased conversion, the

power and the overall efficiency shown in Figure 5.32 become higher. As the operating pressure increases, the driving force for oxygen permeation through the cell increases. This tendency can be explained by the increased oxygen partial pressure in the cathode and the acceleration of reaction rate from the increased methane partial pressure. In addition, the internal cell resistance becomes smaller with increasing the partial pressures of methane and oxygen as shown in Eq. (5.50). It is clear that operation at high pressure is beneficial to SOFC performances; however, other considerations such as problems on seals and mechanical properties of the cells at high pressure should be taken into account for selection of a suitable operating pressure.

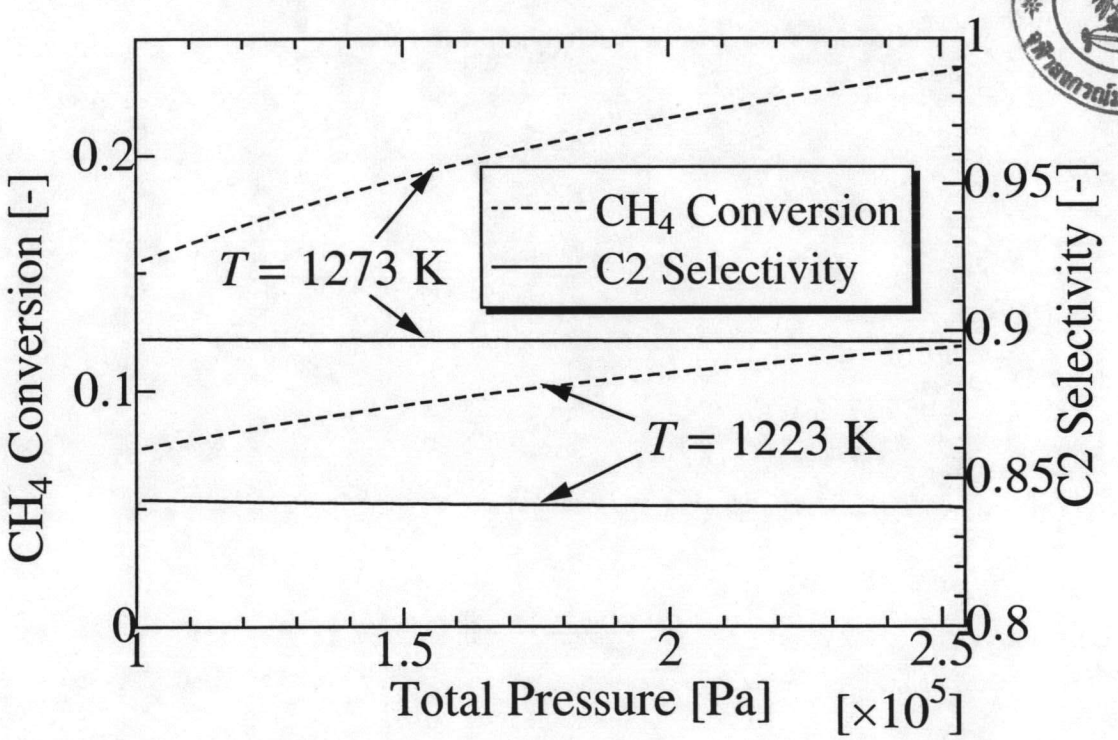

Figure 5.31 Effect of operating pressure on methane conversion and C2 selectivity ($F_{CH_4,0} = 2.0\text{x}10^{-4}$ mol s^{-1}, $W = 4.0\text{x}10^{-5}$ kg, pure methane feed on the anode, air feed on the cathode).

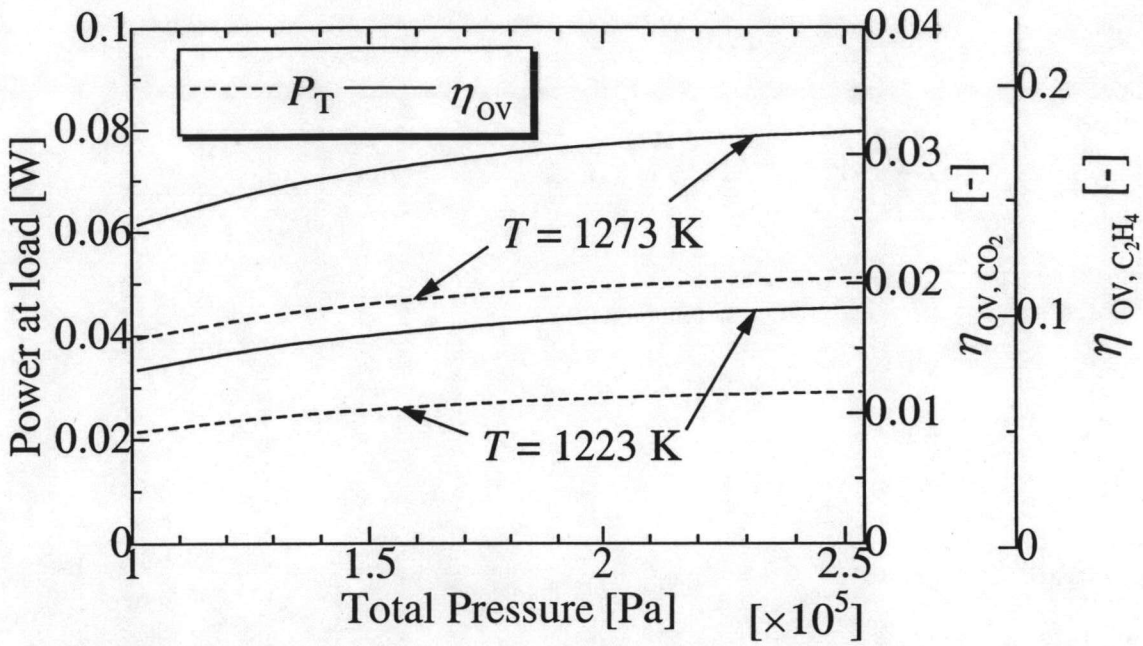

Figure 5.32 Effect of operating pressure on power at load and overall efficiency ($F_{CH_4,0} = 2.0\text{x}10^{-4}$ mol s^{-1}, $W = 4.0\text{x}10^{-5}$ kg, pure methane feed on the anode, air feed on the cathode).

5.4.5 Comparison of SOFC performances among different systems

Typical SOFCs are used for power generation. It is desired to operate the SOFC at high power density. The value of 960 W m^{-2} was reported for the complete oxidation of methane in SOFC with a YSZ electrolyte at 1073 K (Liu *et al.*, 2003). The lower value of 375 W m^{-2} was reported for the partial oxidation of methane to synthesis gas using YSZ electrolytes (Sobyanin *et al.*, 2000). In this study, the maximum power density obtained with pure methane feed at atmospheric pressure and 1273 K is 3.34 W m^{-2}. This value is in the same range reported by other investigators. Guo *et al.* (1999) studied the OCM in tube type SOFC reactor with a YSZ electrolyte of 1 mm thickness. The maximum power density of 3.89 W m^{-2} was obtained at 1003 K. Tagawa *et al.* (1999) studied the OCM in a similar system of this study (LSM/YSZ/LaAlO) but using

a plate type electrolyte. The maximum power density was 13.85 W m^{-2}. This is due to the smaller thickness of the YSZ electrolyte used in their study (0.3 mm).

It is obvious that with the present technology on the OCM in SOFC, the obtained power density is much lower than the conventional SOFC. However, our SOFC system is attractive in that it offers high selectivity to C2 hydrocarbon and electricity is obtained simultaneously.